JGR Space Physics

RESEARCH ARTICLE
10.1029/2023JA031307

Precipitation Rates of Electrons Interacting With Lower-Band Chorus Emissions in the Inner Magnetosphere

Yi-Kai Hsieh[1] **and Yoshiharu Omura**[1]

[1]Research Institute for Sustainable Humanosphere, Kyoto University, Kyoto, Japan

Key Points:

- Electron precipitation rates due to a pair of chorus emissions at different energies and equatorial pitch angles are calculated
- Compared to parallel chorus, oblique chorus results in a greater amount of electron precipitation at energies below several hundred keV
- Pitch angle scattering rates are derived for trapped and untrapped resonant electrons in *n*th cyclotron resonances with oblique chorus

Supporting Information:

Supporting Information may be found in the online version of this article.

Correspondence to:

Y.-K. Hsieh,
yikai_hsieh@rish.kyoto-u.ac.jp

Citation:

Hsieh, Y.-K., & Omura, Y. (2023). Precipitation rates of electrons interacting with lower-band chorus emissions in the inner magnetosphere. *Journal of Geophysical Research: Space Physics*, *128*, e2023JA031307. https://doi.org/10.1029/2023JA031307

Received 10 JAN 2023
Accepted 12 JUN 2023

Author Contributions:

Conceptualization: Yi-Kai Hsieh, Yoshiharu Omura
Formal analysis: Yi-Kai Hsieh
Funding acquisition: Yoshiharu Omura
Investigation: Yi-Kai Hsieh
Methodology: Yi-Kai Hsieh, Yoshiharu Omura
Project Administration: Yoshiharu Omura
Supervision: Yoshiharu Omura
Validation: Yi-Kai Hsieh
Visualization: Yi-Kai Hsieh
Writing – original draft: Yi-Kai Hsieh

Abstract Electrons trapped in the Earth's magnetic field can be scattered by whistler mode chorus emissions and precipitate into the Earth's upper atmosphere. Whistler mode chorus waves propagating in the Earth's inner magnetic field are usually observed with oblique wave normal angles (WNAs). In this study, we apply 12 chorus wave models with four various WNA sets (the maximum WNA are 0°, 20°, 60°, and 90% of resonance cone angles) and three wave amplitude sets (the maximum wave magnetic fields are 2.1 nT, 307 pT, and 49.4 pT) at $L = 4.5$. We use test-particle simulations to trace electrons interacting with the waves and create Green's function sets for electrons initially at kinetic energies (K) 10–6,000 keV and equatorial pitch angles (α) 5°–89°. The simulation results show that in the 2.1 nT cases, the very oblique chorus waves contribute to more electron precipitation than the other three chorus wave models, especially at energies 50–100 keV. Checking the highest initial equatorial pitch angle of the precipitated electrons, we find that the very oblique chorus waves can precipitate electrons with $\alpha > 45°$. In contrast, the other chorus waves can only precipitate electrons with $\alpha < 30°$. Furthermore, the precipitation rates reveal that the anomalous trapping effect, which moves low equatorial pitch angle electrons away from the loss cone, in the oblique cases is much weaker than in the parallel case, resulting in higher precipitation rates. Finally, we derive the pitch angle scattering rates and verify the precipitation by *n*th cyclotron resonances with oblique chorus.

1. Introduction

The population, motion, and distribution of energetic electrons (energies from a few keV to a few MeV) in the Earth's inner magnetosphere are strongly affected by wave-particle interactions (WPI), resulting in energy increasing/decreasing and pitch angle scattering of these electrons. The wave-driven energetic electron precipitation can be led by EMIC waves, whistler mode waves, ULF waves, and the combination of the above waves (e.g., Artemyev et al., 2022; Bashir et al., 2022; Grach & Demekhov, 2020; Hsieh et al., 2022; Kubota & Omura, 2017; Rae et al., 2018; Zhang et al., 2019, 2022, and references therein). Whistler mode chorus emission, a right-hand polarized wave usually with rising or falling frequency variations, is one of the most significant electromagnetic waves that affect electron motions outside the Earth's plasmapause (e.g., Hsieh et al., 2020; Omura, 2021; Sazhin & Hayakawa, 1992; Thorne et al., 2005). Observations show that chorus WPI are reasons for electron precipitation events such as pulsating aurora and microbursts, which is electron precipitation in short timescale (<1 s) and intense energy (tens keV to a few MeV) (A. Breneman et al., 2017; Kasahara et al., 2018; Kurita et al., 2016; Lorentzen et al., 2001; Nishimura et al., 2010; Ozaki et al., 2019). Several simulation studies confirm the detailed mechanisms of chorus wave-driven electron precipitation by test-particle simulations (Miyoshi et al., 2021; Tsai et al., 2022) and particle-in-cell simulations (Hikishima et al., 2010) under the parallel propagation assumption.

Chorus emissions with wave normal angles (WNAs, θ) greater than 10° are usually found in satellite observations. Statistic results of chorus WNAs observed by Cluster and THEMIS show that there are more oblique chorus emissions than parallel/quasi-parallel chorus emissions in the Earth's inner magnetosphere (A. W. Breneman et al., 2009; Li et al., 2011). In addition, chorus emissions with WNA very close to the resonance cone angle are often seen in observations (e.g., Ma et al., 2017; Mourenas et al., 2015). Therefore, to comprehensively understand electron precipitation, we cannot simply assume parallel propagating waves and ignore the oblique propagating effects. It is necessary to take the obliquely propagating waves into account. The most obvious different point between parallel WPI and oblique WPI is the number of resonances. In the parallel WPI only cyclotron resonance occurs, whereas in the oblique WPI there are cyclotron resonance, Landau resonance, and higher harmonic cyclotron resonances. Electrons have more chances to interact with an oblique chorus emission than with a parallel chorus emission.

Long-term electron variations used to be interpreted by diffusion coefficients from the quasi-linear theory (e.g., Lyons et al., 1972; Mourenas et al., 2014; Shprits et al., 2008; Thorne et al., 2005, and references therein). However, the quasi-linear theory is not able to explain actual variations between waves and electrons and cannot describe immediate precipitation seen from observations since it does not solve the equations of motion of particles and ignores the second-order resonance condition. Furthermore, the quasi-linear theory only considers the cyclotron resonance; thus, the zeroth (Landau) and the higher harmonic cyclotron resonances are ignored. Strong chorus wave-driven precipitation is caused by nonlinear resonant effects, especially through cyclotron resonance (Hsieh et al., 2022). Resonances occur when the parallel (with respect to the background magnetic field) velocity of an electron is close to a resonance velocity. The equation of resonance velocities with a harmonic number n is given by

$$V_{R,n} = \frac{1}{k_{\parallel}}\left(\omega - \frac{n\Omega_e}{\gamma}\right), \tag{1}$$

where $k_{\parallel}$ is the wave number parallel to the background magnetic field, ω is the wave frequency, Ω_e is the electron gyro-frequency (here the value is positive), and γ is the Lorentz factor. Two processes belong to nonlinear WPI and contribute to nonlinear pitch angle scattering: (a) nonlinear trapping (also called phase trapping) and (b) nonlinear scattering (also called phase bunching or nonlinear dislocation) (e.g., Bortnik et al., 2008; Omura, 2021; Saito et al., 2012). The processes that lower the equatorial pitch angle of electrons are the nonlinear scattering of the $n \geq 1$ resonances and the nonlinear trapping of the $n < 1$ resonances. The nonlinear trapping via $n = 1$ cyclotron resonance also causes pitch angle decrease for electrons with large pitch angles (>70°) and high energies (>0.5 MeV) (Summers & Omura, 2007), but this kind of WPI does not contribute to electron precipitation. Hence, we do not discuss the condition in this study.

Oblique chorus-driven electron precipitation due to nonlinear WPI has been the subject of several recent studies. For example, Zhang et al. (2022) reported the nonlinear process of precipitation caused by large amplitude and large WNA chorus waves using the CubeSat ELFIN observations, and Chen et al. (2021) simulated the nonducted chorus and the related electron precipitation of tens of keV electrons. Hsieh et al. (2022) confirmed by simulations that through the $n = 0$ Landau resonance oblique chorus emissions cause more energetic electron precipitation than purely parallel chorus emissions, especially for sub-relativistic/relativistic electrons. The study also revealed that a larger WNA causes more precipitation fluxes under the condition that the emissions have the same wave amplitudes. However, the study only investigates chorus emissions with WNA less than 40° at resonance regions. Electron precipitation by a very oblique chorus has not yet been studied by simulation with wide electron energies.

This study investigates electron precipitation for broad initial kinetic energies and equatorial pitch angles interacting with a pair of chorus emissions around a $L = 4.5$ field line by utilizing test particle simulations and the Green's function method. We test lower-band chorus emissions with four WNA settings and three wave amplitudes. We calculate electron precipitation rates by integrating electrons below the loss cone angle ($\alpha_{eq} = 4.56°$) for each Green's function and compare the precipitation rates among all the wave models. We then theoretically derive the equatorial pitch angle change rates for each nth resonance to explain the precipitation processes.

2. Simulation Method and Green's Function Sets

Electron scattering through whistler mode chorus emissions can be traced by the Green's function method (Hsieh et al., 2022; Kubota & Omura, 2018; Omura et al., 2015), which collects possibilities of electron scattering in kinetic energy (K) and equatorial pitch angle (α) from results of test particle simulations with a large number of electrons. In this study we use the Green's function database to check energetic electron precipitation driven by whistler mode chorus.

2.1. Simulation Settings and Wave Models

Overall there are 12 Green's function sets in our database. We have three different wave amplitude sets and four various WNA sets. Figures 1 and 2 display wave models used in this study. Figure 1 shows the wave amplitudes and frequencies at the equator and at $|Lat| = 2°$, where is the terminal of the convective growth of wave amplitudes (Omura et al., 2009). All of the wave models contain subpacket structures generated by chorus equations

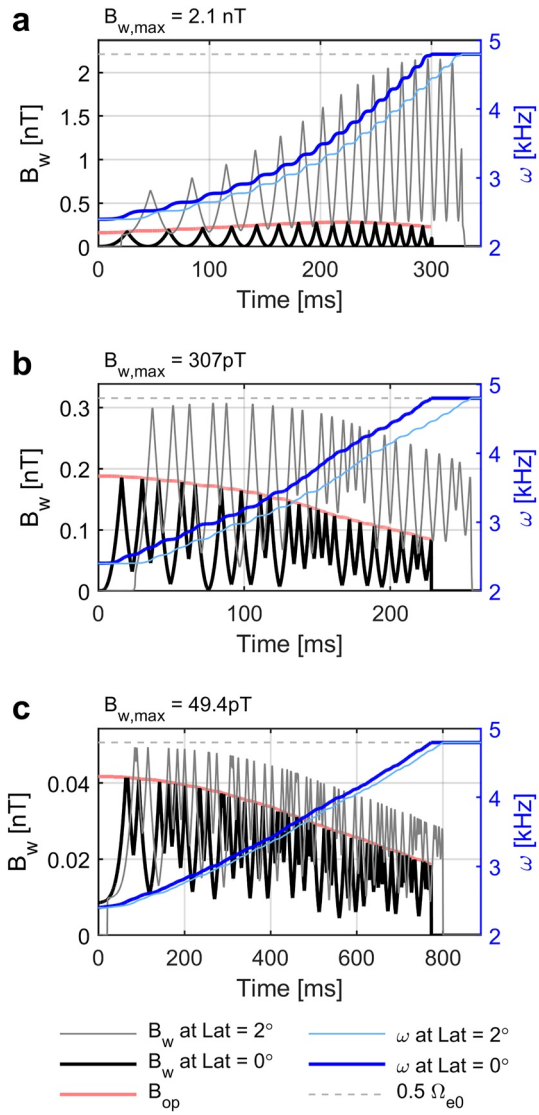

Figure 1. Wave magnetic field amplitudes and frequencies of lower-band chorus waves for the Green's function data sets. We have three different amplitudes sets (a–c). Their maximum amplitudes ($B_{w,\max}$) are (a) 2.1 nT, (b) 307 pT, and (c) 49.4 pT. The black/blue solid lines are wave amplitudes/frequencies at the equator (generation region). The gray/light blue thick lines are wave amplitudes/frequencies at $|Lat| = 2°$, which is the end of the convective growth. The waves start from the equator at $L = 4.5$ and then propagate both northward and southward with group velocity. At $|Lat| > 2°$, the wave amplitudes of wave packets do not change. The pink curves denote the optimum amplitude B_{op} for wave generation. The gray dashed lines indicate the frequency 0.5 Ω_{e0}.

(Equations 106 and 107 of Omura (2021)) at the equator. We turned the sign of Equation 107 of Omura (2021) to negative when the wave amplitudes reach the optimum amplitude B_{op} (Equation 97 of Omura (2021)), which is an amplitude under the optimum condition for nonlinear wave growth (The B_{op} are plotted in pink in Figure 1.). Then, we made the sign positive again before the amplitudes reached the threshold amplitude (Equation 105 of Omura (2021)), which is the minimum amplitude to trigger nonlinear wave growth. To simulate the irregular size of subpackets, the timing of the sign switching from negative to positive is random. The irregular subpackets make the wave models closer to observed subpackets than regular subpackets.

The waves start from the equator at $L = 4.5$ and then propagate both northward and southward with group velocities (Detailed group velocity equation is in Appendix A of Hsieh and Omura (2017)). We update spatial amplitude distributions by solving the advection equation every timestep as

$$\frac{\partial B_w}{\partial t} + V_{g\parallel}\frac{\partial B_w}{\partial h} = -\frac{\mu_0 V_{g\parallel}}{2} J_E. \quad (2)$$

The current J_E is obtained by Equation 16 of Omura et al. (2009) and controls the convective growth of the wave amplitudes. We assume the convective growth only occurs at $|Lat| \le 2°$, and hence $J_E = 0$ at $|Lat| > 2°$. For wave frequencies at $|Lat| > 0°$, we solve

$$\frac{\partial \omega}{\partial t} + V_{g\parallel}\frac{\partial \omega}{\partial h} = 0 \quad (3)$$

to obtain the space-time variations. The maximum wave magnetic field amplitudes $B_{w,\max}$ are 2.1 nT, 307 pT, and 49.4 pT in Figures 1a–1c, respectively, containing three different orders of wave amplitude. The amplitudes are referred to Li et al. (2011) for 50 and 300 pT, and Foster et al. (2017) for 2.1 nT. Profiles of the wave amplitudes and the wave frequencies are shown in Supporting Information.

Input parameters for the amplitude sets are listed in Tables 1 and 2. In this paper, all the subscripts $_\parallel$ ($_\perp$) stand for the parallel (perpendicular) components of variables with respect to the background magnetic field $\mathbf{B}_0$. The duration of each subpacket in Figure 1 is about 10–20 ms, and the subpacket duration of the low frequency parts is longer than that of the higher frequency parts. These wave features agree with observations (i.e., Santolík et al., 2014; Foster et al., 2017). The duration of the waves with different amplitudes are not similar since we have to fit these wave features and the target amplitudes (~50 pT, ~300 pT, and ~2.1 nT.) by adjusting the input parameters in Table 2. Eventually, their wave duration becomes different. However, according to observations (e.g., Shue et al., 2019), the wave duration of every case in this study is still reasonable.

We assume artificial distributions of WNAs in the simulations. WNAs of simulation wave models as functions of latitudes are illustrated in Figure 2. According to our background settings, the angles between the background magnetic field and the wave group velocities of lower-band chorus are always less than 30° (Hsieh & Omura, 2017). Therefore, we can assume the wave packet propagates approximately along the field line. Moreover, Agapitov et al. (2018) reported that the spatial extent of the chorus source is about 1 R_E in the radial direction and about 1.2 hr of MLT in the azimuthal direction. The spatial extent and the group velocity direction indicate that an oblique lower-band chorus can exist near the field line. The blue line (θ_1) represents purely parallel chorus waves, and the other 3 curves stand for oblique chorus waves. The oblique waves are generated at the equator with WNA = 0°, and their WNA increase with propagation. The green line (θ_2) stands for slightly oblique chorus waves with a maximum WNA $\theta_{\max} = 20°$,

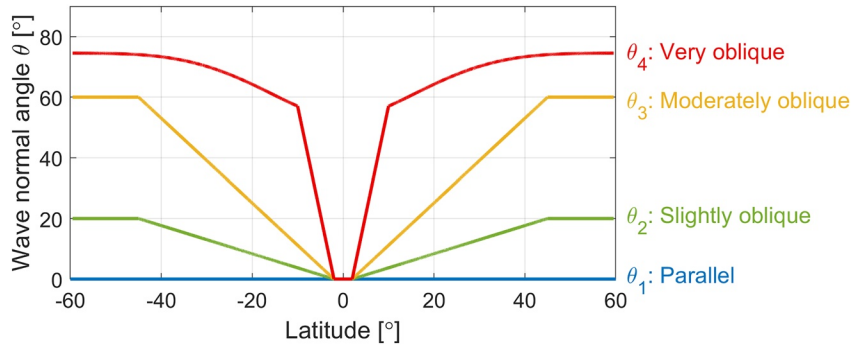

Figure 2. Latitude distributions of wave normal angles (WNAs) θ. We have 4 different settings of WNAs. The blue line shows the parallel case (θ_1). The green line is the slightly oblique case (θ_2) with $\theta = 0°$ at $|Lat| < 2°$, $\theta = 20°$ at $|Lat| > 45°$, and between $|Lat| = 2°$ and 45° the θ is a linear function. The yellow line is the moderately oblique case with $\theta = 0°$ at $|Lat| < 2°$, $\theta = 60°$ at $|Lat| > 45°$, and between $|Lat| = 2°$ and 45° the θ is a linear function. The red curve denotes the very oblique case with $\theta = 0°$ at $|Lat| < 2°$, at $|Lat| > 2°$ the θ is 0.9 times resonance cone angle at $\omega = 0.5\ \Omega_{e0}$, and between $|Lat| = 2°$ and 10° the θ is a linear function.

the yellow line (θ_3) is moderately oblique chorus waves with a $\theta_{max} = 60°$. For θ_2 and θ_3, at $|Lat| \leq 2°$ the WNA is 0°, at $|Lat| \geq 45°$ the WNA is θ_{max}, and at $2° < |Lat| < 45°$ the WNA is a linear function. The red curve (θ_4) denotes very oblique chorus waves, whose WNA is 90% of the resonance cone angle (θ_{res}) for $\omega = 0.5\Omega_{eq}$ at $|Lat| \geq 10°$ and a liner function between 0° and $0.9\theta_{res}$ at $2° \leq |Lat| \leq 10°$.

2.2. Test Particle Simulations

We apply test particle simulations with the wave models described above to obtain the Green's function sets. For a Green's function, 3,600 electrons start at a specific energy and equatorial pitch angle with random initial gyrophases and latitudes. The electron trajectories are obtained from the integration of the equation of motion given by

$$m_0 \frac{\mathrm{d}(\gamma \boldsymbol{v})}{\mathrm{d}t} = q[\mathbf{E}_w + \boldsymbol{v} \times (\mathbf{B}_0 + \mathbf{B}_w)], \tag{4}$$

where m_0 is the rest mass of an electron, $\boldsymbol{v}$ is the electron velocity, q is the electric charge, $\mathbf{E}_w$ is the wave electric field, $\mathbf{B}_0$ is the ambient magnetic field, and $\mathbf{B}_w$ is the wave magnetic field. A Green's function set gathers results of test particle simulations with one wave model described above. There are 51,000 Green functions in a Green's function set with initial energies from 10 keV to 6 MeV (interval 10 keV) and equatorial pitch angles from 5° to 89° (interval 1°). According to $L = 4.5$, the loss cone angle θ_{loss} is 4.56° corresponding to an altitude of 100 km from the Earth's surface. After being affected by a pair of chorus emissions, electrons inside the loss cone are treated as loss electrons.

3. Simulated Precipitation Rates

The electron precipitation rates in this study are defined by the simulation input and the results. For a Green's function, electrons scatter in kinetic energies and equatorial pitch angles after interacting with a pair of the

Table 1
General Input Parameters

Parameters	Normalized value	Real value
L-shell (L)		4.5
Equatorial background magnetic field (B_{0eq})		342 nT
Equatorial electron gyrofrequency (Ω_{e0})		9.48 kHz
Electron plasma frequency (ω_{pe})	$4\ \Omega_{e0}$	37.9 kHz
Cold electron density (n_e)		18/cc
Wave frequency (ω)	$0.25 - 0.5\ \Omega_{e0}$	2.37 − 4.74 kHz
Charge to mass ratio (q/m_0)	$-1e/m_e$	-1.76×10^{11} C/kg

Table 2
Input Parameters for Three Wave Sets

$B_{w,\max}$	Normalized $B_{w,\max}$	n_h	$V_{t\parallel}$	$V_{\perp 0}$	Q	τ
2.1 nT	0.006 Ω_{e0}	0.005 n_e	0.15 c	0.3 c	0.5	0.5
307 pT	0.00088 Ω_{e0}	0.0018 n_e	0.2 c	0.4 c	0.5	0.5
49.4 pT	0.00015 Ω_{e0}	0.001 n_e	0.2 c	0.4 c	0.2	0.5

Note. $B_{w,\max}$, Maximum wave magnetic field amplitude; n_h, Source electron density; $V_{t\parallel}$, Parallel thermal velocity of source electrons; $V_{\perp 0}$, Averaged perpendicular velocity of source electrons; Q, Depth of an electron hole; τ, Nonlinear transition time to nonlinear trapping time ratio.

given emissions. The denominator of the electron precipitation rate is the number of the input electrons of a Green's function, and the numerator is the number of electrons in the loss cone after the interactions. In other words, considering a group of electrons at a certain energy and an equatorial pitch angle, the precipitation rate estimates the percentage of the electrons being precipitated by a chorus wave packet. Figure 3 plots the precipitation rates for the $B_{w\max} = 2.1$ nT cases. Figures 3a–3d are respectively the precipitation rates of Cases θ_1, θ_2, θ_3, and θ_4. Figure 3e shows the precipitation rates for all equatorial pitch angles as functions of the initial kinetic energies. N_L means the number of loss electrons of each initial energy, and N_p is the number of the input electrons for each energy. The blue, green, violet, and dark orange curves stand for Cases θ_1, θ_2, θ_3, and θ_4, respectively.

Obviously, Figure 3e shows that larger WNA waves cause more electron precipitation at energy less than 500 keV. For energy greater than 500 keV, the Case θ_4 still makes the most extensive precipitation, but the precipitation of the other cases is almost the same. For the parallel case (Figure 3a), the highest precipitation angles (HPA) for low energies are higher than the HPA for high energies. Namely, low-energy electrons (<100 keV) have more chances of being precipitated than high-energy electrons (~MeV) have. It must be pointed out that there is a slot around K = tens of keV and $\alpha_{eq} = 10°$. This slot is probably due to the anomalous trapping mechanism introduced by Kitahara and Katoh (2019). A low equatorial pitch angle electron is trapped by a wave and its equatorial pitch angle becomes higher. The slot can be found in the other cases, but their sizes are much smaller than that of the parallel case, indicating that the multiple resonances effect in oblique WPI weakens the anomalous trapping. The anomalous trapping lowers precipitation rates of the parallel case at tens of keV. In Figure 3e, we find that the blue curve is much lower than the other curves at energies tens of keV.

Compared with Figure 3a, Figures 3b and 3c (oblique cases θ_2 and θ_3) show additional bulges around (K, α) = (150 keV, 20°). The bulges are due to the multiple resonances effect, particularly the $n = 2$ resonance. We will discuss the mechanism later in Section 4.

Figure 3d is the most special case with very large WNAs. There is a distinct precipitation pattern around K = 30–150 keV and α = 30°–50°, which makes the Case θ_4 the strongest precipitation case. The HPA of the

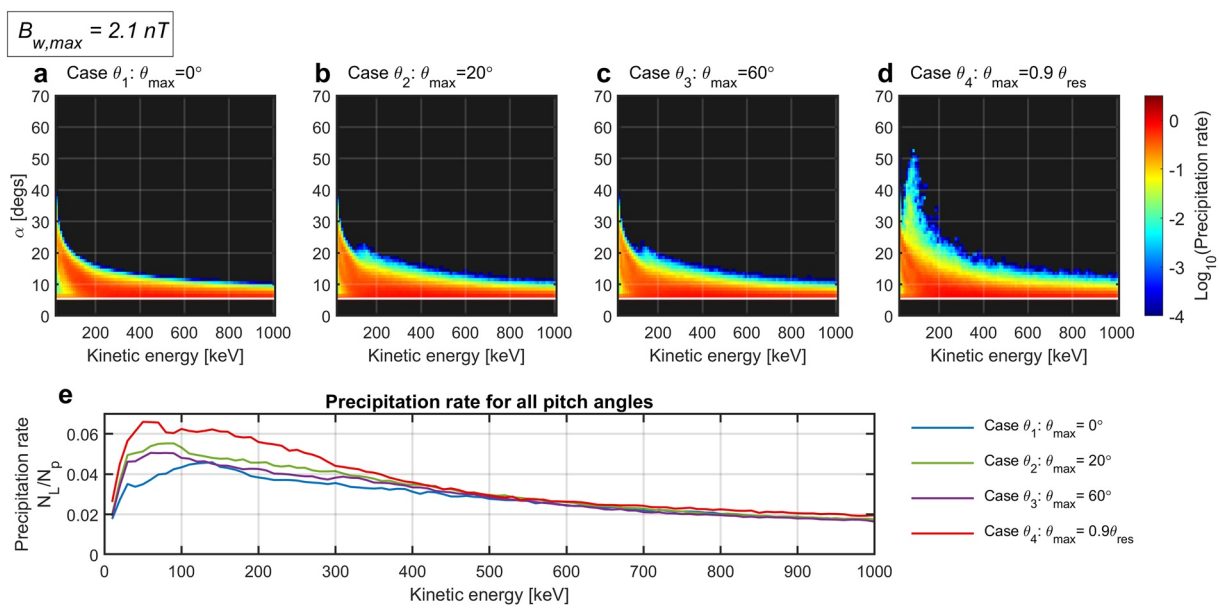

Figure 3. Precipitation rates for electrons interacting with a pair of chorus emissions shown in Figure 1a. (a–d) Electron precipitation rates as functions of initial kinetic energies and equatorial pitch angles with different wave normal angle settings Case θ_1–Case θ_4. The white lines denote the loss cone angle 4.56°. No electron precipitates from the black region. (e) Precipitation rate for all pitch angles as functions of kinetic energy. Blue, green, violet, and dark orange curves stand for Cases θ_1, θ_2, θ_3, and θ_4, respectively.

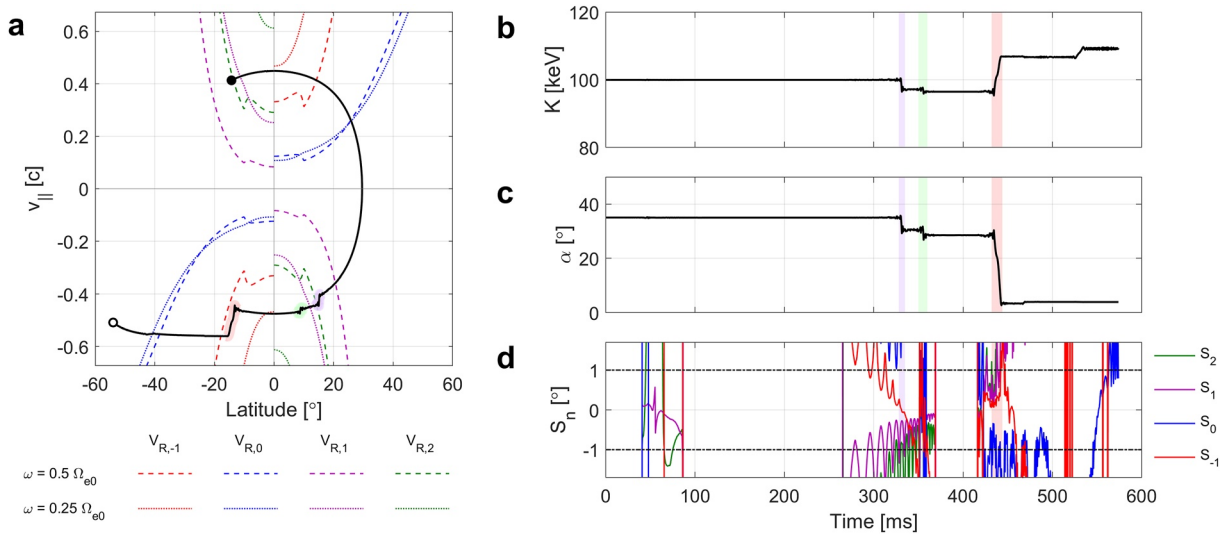

Figure 4. An example of a precipitated electron initially at $K = 100$ keV and $\alpha = 35°$. (a) Electron trajectories in a *Lat*–$v_{\parallel}$ phase space. Specific resonances can be recognized in this plot by checking the resonance velocities V_{Rn} with different n. (b) Time variations of the kinetic energy K. (c) Time variations of the equatorial pitch angle α. (d) Inhomogeneity factors for $n = -1$ (red), $n = 0$ (blue), $n = 1$ (purple), and $n = 2$ (green). Areas shaded with light purple, green, and red colors in each panel point out the periods when the electron undergoes $n = 1$, $n = 2$, and $n = -1$ resonances, respectively.

Case θ_4 is much higher than those of the other cases. Namely, electrons can precipitate from a high initial equatorial pitch angle when interacting with a very oblique chorus wave. Figure 3e shows that at $K < 100$ keV, the precipitation rates of the Case θ_4 are about 1.5 times those of the Case θ_1 and about 1.2 times those of the Case θ_2 and θ_3. We check the detailed trajectories of electrons belonging to the distinct precipitation pattern and find that the precipitation is caused by nonlinear trapping of $n = -1$ cyclotron resonance. Figure 4 shows an example of precipitated electron starting at $K = 100$ keV and $\alpha = 35°$ in Figure 3d. In the other wave cases, electrons cannot be precipitated from these energy and equatorial pitch angle.

Figure 4a is a *Lat*–$v_{\parallel}$ trajectory. The dotted lines and the dashed lines denote the resonance velocities V_{Rn} for $\omega = 0.25$ and $0.5\ \Omega_{e0}$, respectively. The red, blue, green, and purple colors stand for harmonic numbers -1, 0, 1, and 2, respectively. Figures 4b and 4c respectively show the time variations of the kinetic energy and equatorial pitch angle of the electron. The inhomogeneity factors S_n for $n = -1$ to 2 are plotted in Figure 4d. The color order of the resonances in Figure 4d is the same as that in Figure 4a. The equation of S_n is given later in Equation 34. Checking these plots, we can easily find that the primary precipitation occurs in the light red area. The *Lat*–$v_{\parallel}$ trajectory follows the V_{R-1} curve, and the $|S_{-1}|$ is less than 1, indicating that the nonlinear trapping via $n = -1$ cyclotron resonance occurs in the light area and is the primary process contributing to the electron precipitation. The electron undergoes 2 more resonances, which are nonlinear scattering via $n = 1$ cyclotron resonance (light purple area) and nonlinear scattering via $n = 2$ cyclotron resonance (light green area), before the $n = -1$ cyclotron resonance occurs. However, the $n = 2$ and $n = 1$ cyclotron resonances do not make critical decreasing of the electron pitch angle.

Figure 5 shows precipitation rates of the $B_{w\max} = 307$ and 49.4 pT cases. The figure configuration is similar to Figure 3. In Figure 5i, the solid and dotted curves stand for the $B_{w\max} = 307$ and 49.4 pT cases, respectively. Obviously, the precipitation rates in Figures 5a–5d are very similar, and the rates in Figures 5e–5h are also very close. The results signify that the nonlinear interactions of $n \neq 1$ resonances are very weak for waves with amplitude around tens of pT to a few hundred pT. The figure also indicates that the HPA is highly affected by wave amplitudes. According to Figures 3 and 5, we have three general conclusions about chorus-induced electron precipitation: (a) The wave amplitude is the most critical parameter controlling the electron precipitation rate. A larger wave amplitude results in more electron precipitation. (b) The precipitation rates of tens of keV electrons are higher than those of hundreds of keV electrons, except for purely parallel waves with a large amplitude, in which the anomalous trapping is strong. (c) A rough tendency is that at low electron energy the HPA is high, and at high electron energy the HPA is low.

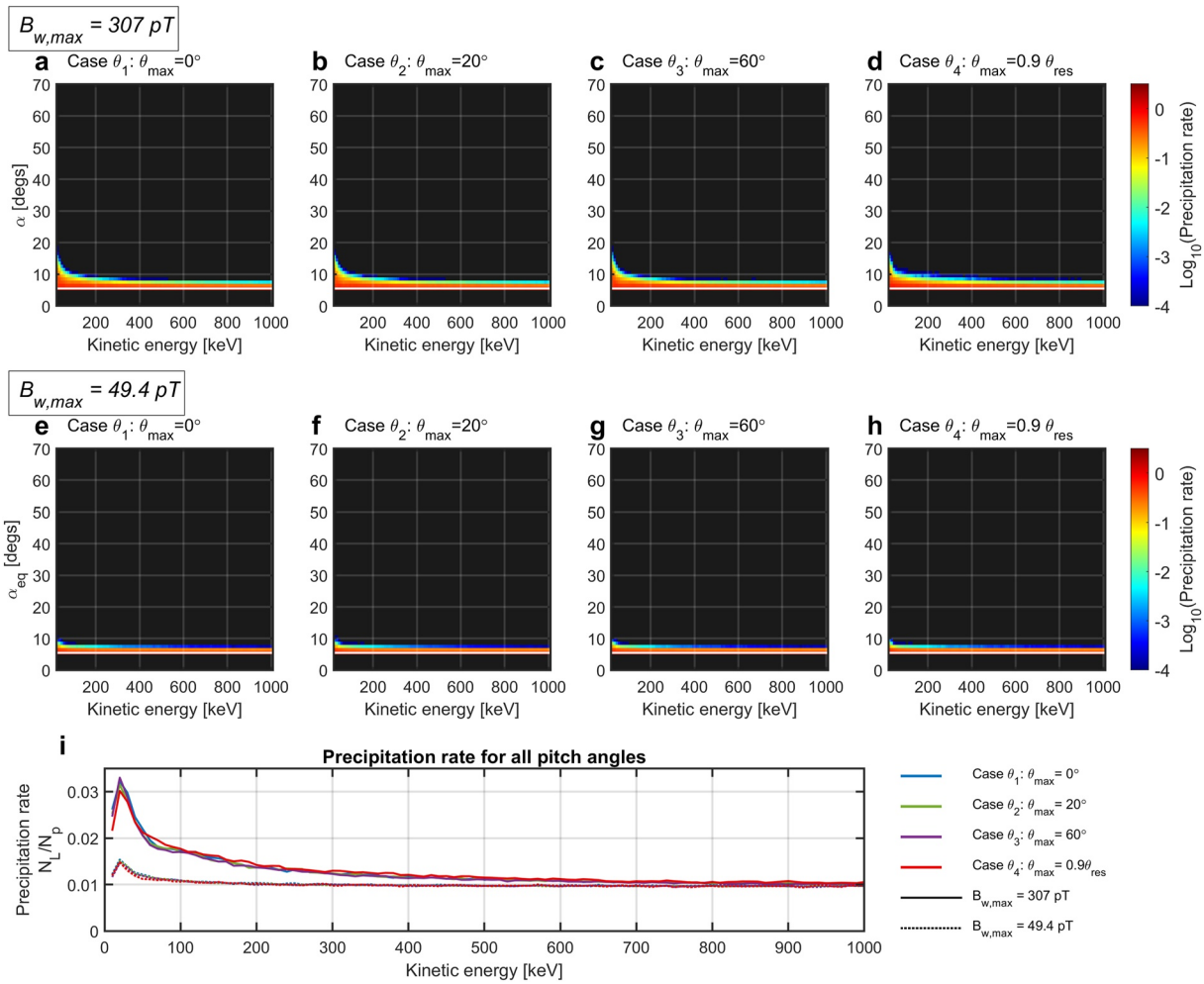

Figure 5. Precipitation rates for electrons interacting with a pair of chorus emissions shown in Figures 1b and 1c. (a–h) Figure configurations are the same as in Figure 3. (i) Precipitation rate among all pitch angles as functions of kinetic energies. Blue, green, violet, and dark orange curves stand for Cases θ_1, θ_2, θ_3, and θ_4, respectively. The solid lines show the $B_{w,\max} = 307$ pT cases, and the dotted lines show the $B_{w,\max} = 49.4$ pT cases.

4. Discussion

We theoretically calculate the time derivative of equatorial pitch angles of resonant electrons to verify the effects of different resonances on electrons. We check if the theoretical estimations agree with the simulation results in this section.

4.1. Theoretical Equatorial Pitch Angle Scattering Rates

Considering the field aligned coordinates, with electron parallel velocity $v_\parallel$, electron perpendicular velocity $v_\perp$, electron gyro-phase ϕ, wave phase ψ, the gradient of the ambient magnetic field $\mathrm{d}\Omega_e/\mathrm{d}h$, left-handed polarized wave magnetic field amplitude $\Omega_L = eB_L^w/m_0$, right-handed polarized wave magnetic field amplitude $\Omega_R = eB_R^w/m_0$, parallel wave magnetic field $B_\parallel^w$, and parallel wave electric field amplitude $E_\parallel^w$, the equation of motion (Equation 4) is separated as (Nunn & Omura, 2015; Omura, 2021)

$$\frac{\mathrm{d}(\gamma v_\parallel)}{\mathrm{d}t} = \Omega_R v_\perp \sin(\phi - \psi) + \Omega_L v_\perp \sin(\phi + \psi) - \frac{eE_\parallel^w}{m_0}\sin\phi - \frac{\gamma v_\perp^2}{2\Omega_e}\frac{\mathrm{d}\Omega_e}{\mathrm{d}h}, \tag{5}$$

$$\frac{\mathrm{d}(\gamma v_\perp)}{\mathrm{d}t} = \Omega_R(U_R - v_\parallel)\sin(\phi - \psi) + \Omega_L(U_L - v_\parallel)\sin(\phi + \psi) + \frac{\gamma v_\perp v_\parallel}{2\Omega_e}\frac{\mathrm{d}\Omega_e}{\mathrm{d}h}, \tag{6}$$

$$\frac{\mathrm{d}\phi}{\mathrm{d}t} = \frac{\Omega_e}{\gamma} + \frac{\Omega_R}{\gamma v_\perp}(U_R - v_\parallel)\cos(\phi - \psi) + \frac{\Omega_L}{\gamma v_\perp}(U_L - v_\parallel)\cos(\phi + \psi) - \frac{eB_\parallel^w}{\gamma m_0}\cos\psi, \tag{7}$$

where $U_L = E_L^w / B_L^w$ and $U_R = E_R^w / B_R^w$ are the left-handed and right-handed polarized electric field to magnetic field ratios, respectively. The last terms of Equations 5 and 6 are effects of gradient of the background magnetic field. The wave phase ψ observed by an electron with a gyrophase ϕ is written as

$$\psi = \omega t - k_\parallel h - k_\perp r_c \sin\phi + const. = \psi_B - \beta\sin\phi, \tag{8}$$

where $k_\parallel$ and $k_\perp$ are respectively the parallel and perpendicular wave numbers, ψ_B is the wave phase at the electron guiding center, $r_c = \gamma v_\perp / \Omega_e$ is the gyro-radius, h is the distance from the equator along a field line, and $\beta = r_c k_\perp$. We have the relation regarding the Bessel functions of the first kind J_n as

$$e^{i(\phi-\psi)} = e^{i(\phi-\psi_B)} e^{i\beta\sin\phi} = e^{i(\phi-\psi_B)} \sum_{n=-\infty}^{\infty} J_n(\beta) e^{in\phi} = \sum_{n=-\infty}^{\infty} J_n(\beta) e^{i[(n+1)\phi-\psi_B]}. \tag{9}$$

Replacing $n+1$ by n and n by $n-1$ of Equation 9 and only taking the imaginary part, we obtain

$$\sin(\phi - \psi) = \sum_{n=-\infty}^{\infty} J_{n-1}(\beta)\sin(n\phi - \psi_B) = \sum_{n=-\infty}^{\infty} J_{n-1}(\beta)\sin\zeta_n, \tag{10}$$

where

$$\zeta_n = n\phi - \psi_B. \tag{11}$$

Similarly, we have

$$e^{-i(\phi+\psi)} = e^{-i(\phi+\psi_B)} e^{i\beta\sin\phi} = e^{i(\phi+\psi_B)} \sum_{n=-\infty}^{\infty} J_n(\beta) e^{in\phi} = \sum_{n=-\infty}^{\infty} J_n(\beta) e^{i[(n-1)\phi-\psi_B]}, \tag{12}$$

$$\sin(\phi + \psi) = -\sum_{n=-\infty}^{\infty} J_{n+1}(\beta)\sin\zeta_n, \tag{13}$$

$$e^{-i\psi} = e^{i(\beta\sin\phi-\psi_B)} = e^{-i\psi_B} \sum_{n=-\infty}^{\infty} J_n(\beta) e^{in\phi} = \sum_{n=-\infty}^{\infty} J_n(\beta) e^{i\zeta_n}, \tag{14}$$

and

$$\sin(\psi) = -\sum_{n=-\infty}^{\infty} J_n(\beta)\sin\zeta_n. \tag{15}$$

Substituting Equations 10, 13, and 15 into Equations 5 and 6, we obtain

$$\frac{\mathrm{d}(\gamma v_\parallel)}{\mathrm{d}t} = \frac{1}{k_\parallel}\sum_{n=-\infty}^{\infty} \omega_{t,n}^2 \sin\zeta_n - \frac{\gamma v_\perp^2}{2\Omega_e}\frac{\mathrm{d}\Omega_e}{\mathrm{d}h}, \tag{16}$$

$$\frac{\mathrm{d}(\gamma v_\perp)}{\mathrm{d}t} = \frac{1}{k_\parallel}\sum_{n=-\infty}^{\infty} \omega_{s,n}^2 \sin\zeta_n + \frac{\gamma v_\perp v_\parallel}{2\Omega_e}\frac{\mathrm{d}\Omega_e}{\mathrm{d}h}, \tag{17}$$

where

$$\omega_{t,n}^2 = \frac{ek_\parallel}{m_0}\left[E_\parallel^w J_n(\beta) + v_\perp B_R^w J_{n-1}(\beta) - v_\perp B_L^w J_{n+1}(\beta)\right], \tag{18}$$

$$\omega_{s,n}^2 = \frac{ek_\parallel}{m_0}\left[B_R^w (U_R - v_\parallel) J_{n-1}(\beta) - B_L^w (U_L - v_\parallel) J_{n+1}(\beta)\right]. \tag{19}$$

The time derivative of kinetic energy is

$$\frac{\mathrm{d}K}{\mathrm{d}t} = \frac{\mathrm{d}}{\mathrm{d}t}\left[m_0c^2(\gamma-1)\right] = -e\mathbf{E}\cdot\boldsymbol{v} = -\mathrm{e}\left[E_{\parallel}^{w}v_{\parallel}\sin\psi - E_{R}^{w}v_{\perp}\sin(\phi-\psi) - E_{L}^{w}v_{\perp}\sin(\phi-\psi)\right]. \tag{20}$$

Hence, the time derivative of the Lorentz factor is written as

$$\frac{\mathrm{d}\gamma}{\mathrm{d}t} = \frac{1}{c^2}\sum_{n=-\infty}^{\infty} W_n \sin\zeta_n, \tag{21}$$

where

$$W_n = \frac{e}{m_0}\left[E_{\parallel}^{w}v_{\parallel}J_n(\beta) + E_{R}^{w}v_{\perp}J_{n-1}(\beta) - E_{L}^{w}v_{\perp}J_{n+1}(\beta)\right]. \tag{22}$$

Substituting Equation 21 into Equations 16 and 17, we get

$$\frac{\mathrm{d}v_{\parallel}}{\mathrm{d}t} = \frac{1}{\gamma k_{\parallel}}\sum_{n=-\infty}^{\infty}\left(\omega_{t,n}^2 - \frac{v_{\parallel}k_{\parallel}W_n}{c^2}\right)\sin\zeta_n - \frac{\gamma v_{\perp}^2}{2\Omega_e}\frac{\mathrm{d}\Omega_{\mathrm{e}}}{\mathrm{d}h}, \tag{23}$$

$$\frac{\mathrm{d}v_{\perp}}{\mathrm{d}t} = \frac{1}{\gamma k_{\parallel}}\sum_{n=-\infty}^{\infty}\left(\omega_{s,n}^2 - \frac{v_{\perp}k_{\parallel}W_n}{c^2}\right)\sin\zeta_n + \frac{\gamma v_{\perp}v_{\parallel}}{2\Omega_e}\frac{\mathrm{d}\Omega_{\mathrm{e}}}{\mathrm{d}h}. \tag{24}$$

Applying $\eta = v_{\perp}/v_{\parallel}$, the time derivative of the local pitch angle $\alpha_h = \tan^{-1}(v_{\perp}/v_{\parallel})$ is written as

$$\begin{aligned}\frac{\mathrm{d}\alpha_h}{\mathrm{d}t} &= \frac{\mathrm{d}\alpha_h}{\mathrm{d}\eta}\frac{\mathrm{d}\eta}{\mathrm{d}t}\\ &= \frac{1}{1+\eta^2}\left(\frac{1}{v_{\parallel}}\frac{\mathrm{d}v_{\perp}}{\mathrm{d}t} - \frac{v_{\perp}}{v_{\parallel}^2}\frac{\mathrm{d}v_{\perp}}{\mathrm{d}t}\right).\end{aligned} \tag{25}$$

Since

$$\frac{1}{1+\eta^2} = \frac{v_{\parallel}^2}{v^2}, \tag{26}$$

substituting Equations 23 and 24 into Equation 25, it yields

$$\begin{aligned}\frac{\mathrm{d}\alpha_h}{\mathrm{d}t} &= \frac{v_{\parallel}^2}{v^2}\left\{\frac{1}{v_{\parallel}}\left[\frac{1}{\gamma k_{\parallel}}\sum_{n=-\infty}^{\infty}\left(\omega_{s,n}^2 - \frac{v_{\perp}k_{\parallel}W_n}{c^2}\right)\sin\zeta_n + \frac{v_{\perp}v_{\parallel}}{2\Omega_e}\frac{\mathrm{d}\Omega_{\mathrm{e}}}{\mathrm{d}h}\right]\right.\\ &\quad\left. - \frac{v_{\perp}}{v_{\parallel}^2}\left[\frac{1}{\gamma k_{\parallel}}\sum_{n=-\infty}^{\infty}\left(\omega_{t,n}^2 - \frac{v_{\parallel}k_{\parallel}W_n}{c^2}\right)\sin\zeta_n - \frac{v_{\perp}^2}{2\Omega_e}\frac{\mathrm{d}\Omega_{\mathrm{e}}}{\mathrm{d}h}\right]\right\}\\ &= \sum_{n=-\infty}^{\infty}\left(v_{\parallel}\omega_{s,n}^2 - v_{\perp}\omega_{t,n}^2\right)\frac{\sin\zeta_n}{\gamma k_{\parallel}v^2} + \frac{v_{\perp}}{2\Omega_e}\frac{\mathrm{d}\Omega_{\mathrm{e}}}{\mathrm{d}h}.\end{aligned} \tag{27}$$

The first summation term of Equation 27 is the wave-driven term, and the second term is the magnetic field gradient contributed term. The relation between equatorial pitch angle α and local pitch angle α_h is

$$\alpha = \sin^{-1}\left(\sqrt{\frac{B_{eq}}{B_h}}\sin\alpha_h\right), \tag{28}$$

where B_h is the magnitude of the local background magnetic field, and along the same field line, the magnitude of the equatorial magnetic field is B_{eq}. Since the magnetic field gradient does not affect the variations of equatorial pitch angles, we ignore the $\mathrm{d}\Omega_e/\mathrm{d}h$ terms in the following derivations. Taking the wave-driven term of Equation 27 and a specific nth resonance into account, we obtain the equatorial pitch angle scattering rate of an electron undergoing nth resonance as

$$\begin{aligned}\frac{\mathrm{d}\alpha}{\mathrm{d}t} &= \frac{\mathrm{d}\alpha}{\mathrm{d}\alpha_h}\frac{\mathrm{d}\alpha_h}{\mathrm{d}t}\\ &= \left(v_{\parallel}\omega_{s,n}^2 - v_{\perp}\omega_{t,n}^2\right)\frac{\sin\zeta_n}{\gamma k_{\parallel}v^2}\sqrt{1-\frac{B_h}{B_{eq}}\sin^2\alpha}\sqrt{\frac{B_{eq}}{B_h}}\frac{1}{\cos\alpha}.\end{aligned} \tag{29}$$

For a resonant electron,

$$v_{\parallel} \simeq V_{R,n}. \tag{30}$$

We have the relation

$$\sqrt{1-\frac{B_h}{B_{eq}}\sin^2\alpha} = \cos\alpha_h = \frac{v_{\parallel}}{v}. \tag{31}$$

Therefore, substituting Equations 30 and 31 into Equation 29, the equatorial pitch angle scattering rate is approximately

$$\frac{\mathrm{d}\alpha}{\mathrm{d}t} \simeq \left(V_{R,n}\omega_{s,n}^2 - v_{\perp}\omega_{t,n}^2\right)\frac{V_{R,n}}{\gamma k_{\parallel} v^3}\frac{\sin\zeta_n}{\cos\alpha}\sqrt{\frac{B_{eq}}{B_h}}. \tag{32}$$

This paper discusses the theoretical equatorial pitch angle scattering rates in two conditions: nonlinearly trapped electrons and untrapped resonant electrons.

4.2. Nonlinearly Trapped Electrons

When an electron undergoes the nonlinear trapping, the second-order resonance condition should be satisfied (e.g., Nunn, 1974; Nunn & Omura, 2015). The second-order resonance condition is given by

$$\sin\zeta_n = -S_n. \tag{33}$$

The inhomogeneity factor S_n is given by (See Appendix A for detailed derivations)

$$S_n = \frac{1}{\Omega_{t,n}^2}\left[\left(\frac{2V_{R,n}}{V_{g\parallel}}-1\right)\frac{\partial\omega}{\partial t} + V_{R,n}^2\frac{\partial k_{\parallel}}{\partial h} + \left(\frac{n}{\gamma}V_{R,n} - \frac{k_{\parallel}v_{\perp}^2}{2\Omega_e}\right)\frac{\partial\Omega_e}{\partial h}\right], \tag{34}$$

where

$$\Omega_{t,n}^2 = \frac{1}{\gamma}\left(\omega_{t,n}^2 - \omega\Omega_{d,n}\right), \tag{35}$$

and

$$\Omega_{d,n} = \frac{e}{m_0 c^2}\left[v_{\parallel}E_{\parallel}^w J_n(\beta) + v_{\perp}E_R^w J_{n-1}(\beta) - v_{\perp}E_L^w J_{n+1}(\beta)\right]. \tag{36}$$

The $\partial\omega/\partial t$ in Equation 34 is the frequency sweep rate. The $\partial k_{\parallel}/\partial h$ is the gradient of parallel wave numbers, a term containing the frequency sweep rates, the gradient of wave normal angels, and the gradient of background parameters such as magnetic field and plasma frequencies. It is not easy to obtain $\partial k_{\parallel}/\partial h$ from in situ observations since satellites cannot orbit along a field line measuring these parameters and obtaining the gradient of the required parameters. If we assume the WNAs and the plasma frequencies do not change much along a field line, we can omit $\partial\theta/\partial h$ and $\partial\omega_{pe}/\partial h$ terms in $\partial k_{\parallel}/\partial h$, and then the S_n can be described by the contribution of the frequency sweep rate $\partial\omega/\partial t$ and the gradient of the background magnetic field $\partial\Omega_e/\partial h$ as

$$S_n = \frac{1}{\Omega_{t,n}^2}\left\{-\left(\frac{V_{R,n}}{V_{g\parallel}}-1\right)^2\frac{\partial\omega}{\partial t} + \left[\frac{n}{\gamma}V_{R,n} - \frac{k_{\parallel}v_{\perp}^2}{2\Omega_e} - \frac{V_{R,n}^2}{2}\left(\frac{\omega_{pe}}{c}\right)^3\left(\frac{\Omega_e}{\omega}\cos\theta - 1\right)^{-\frac{3}{2}}\frac{\cos^2\theta}{\omega}\right]\frac{\partial\Omega_e}{\partial h}\right\}. \tag{37}$$

The derivation and the detailed explanation of Equation 37 are also shown in Appendix A. Omura et al. (2019) and Omura (2021) have reported the inhomogeneity factors for quasi-parallel chorus waves. However, they are not valid for oblique chorus waves since they applied the parallel chorus wave dispersion relation in the derivations. We improve the derivation of the inhomogeneity factor S_n so that Equations 34 and 37 are suitable for whistler mode waves at any WNA.

To obtain the $\mathrm{d}\alpha/\mathrm{d}t$, we calculate electron parallel velocities $v_{\parallel}$ along an $L = 4.5$ field line (the same as the simulations described above) under the adiabatic motion for an electron with a specific equatorial pitch angle α and

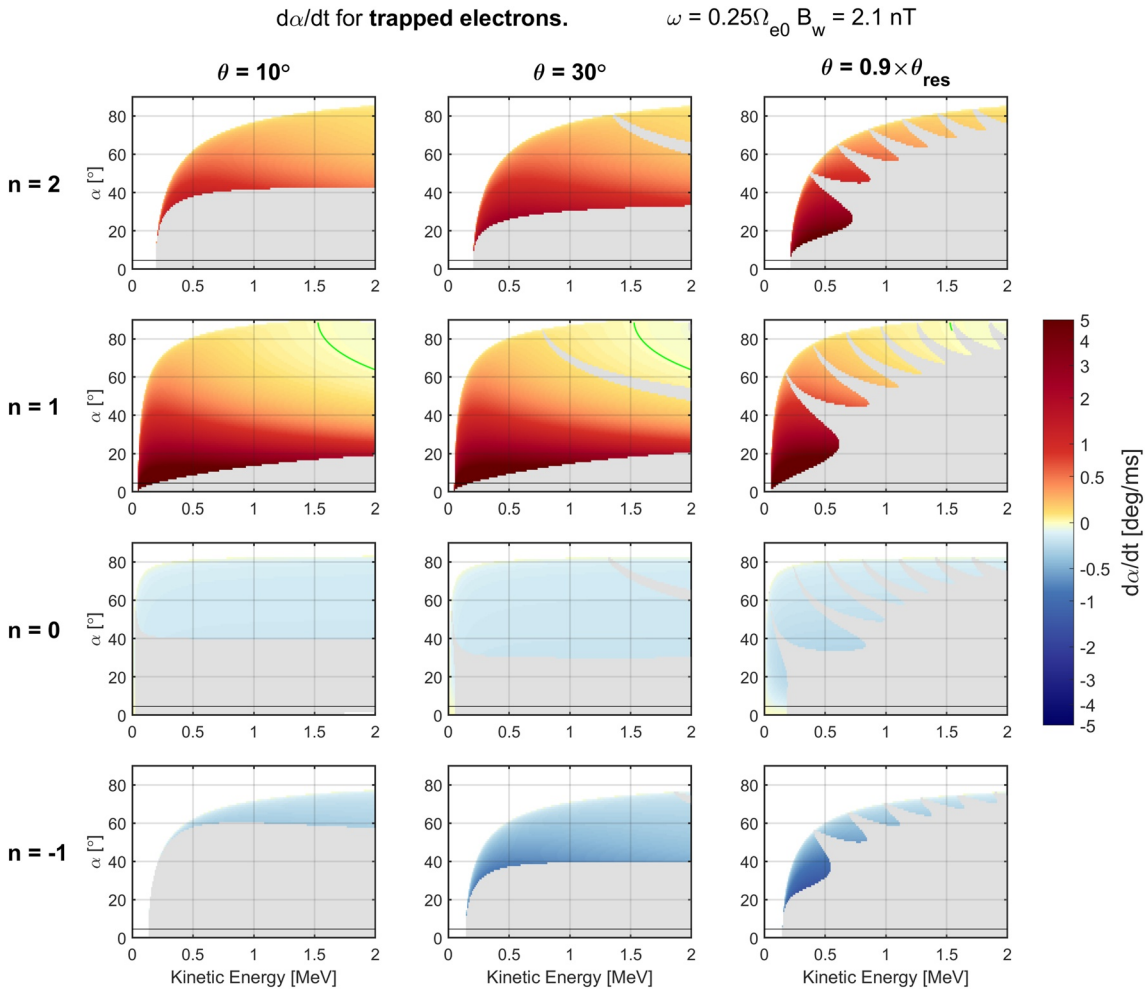

Figure 6. Equatorial pitch angle scattering rates of nonlinearly trapped electrons for a total wave amplitude 2.1 nT and a wave frequency 0.25 Ω_{e0}. The white area means equatorial pitch angle and energy ranges where the electron $v_{\parallel}$ never reaches the resonance velocity $V_{R,n}$ hence the resonance does not occur. The gray area denotes where the absolute value of the inhomogeneous factor is greater than 1 (nonlinear trapping cannot happen). The green curves indicate $d\alpha/dt = 0$.

kinetic energy K, and we also calculate the resonance velocity V_R along the field line. Then, we find a position h_r, where the resonance occurs ($v_{\parallel} = V_R$). Figure 6 shows the $d\alpha/dt$ as functions of the initial kinetic energies and equatorial pitch angles of trapped electrons at h_r with a wave amplitude 2.1 nT (0.6% of B_{0eq}), a wave frequency 0.25 Ω_{e0}, a frequency sweep rate $\partial\omega/\partial t = 0$, and a constant WNA. We separate $d\alpha/dt$ into nth resonances for n from −1 to 2 and plot three different WNAs ($\theta = 10°$, 30° and $0.9 \times \theta_{res}$). We do not plot $d\alpha/dt$ of parallel waves ($\theta = 0°$) because there are no $n = -1$, 0, and 2 resonances in parallel WPI, and the $d\alpha/dt$ with $n = 1$ and $\theta = 0°$ is almost the same as that with $(n, \theta) = (1, 10°)$. Here we set $\sin\zeta_n = -S_n$ in Equation 32 representing nonlinearly trapped electrons. Warm colors show increasing α after the resonances, and cold colors denote decreasing α. The white areas are positions where the electron $v_{\parallel}$ cannot reach the V_{Rn} at all latitudes. The gray parts are $|S_n| > 1$, indicating that the nonlinear trapping cannot happen. The black solid lines denote the loss cone angle $\alpha_{loss} = 4.56°$. The green solid curves point out where $d\alpha/dt = 0$, indicating the turning of increasing or decreasing α. Similar figure for $\omega = 0.4\ \Omega_{e0}$ is plotted in Figure 7.

Figures 6 and 7 tell that, generally, the nonlinear trapping via $n \geq 1$ resonances causes increasing of α, except for high-energy and high-equatorial pitch angle electrons as shown in the right-top corner (the yellow parts righter than the green curves) of all subplots in the second rows ($n = 1$). This tendency agrees with relativistic turning acceleration (Omura et al., 2007) and ultra-relativistic acceleration (Summers & Omura, 2007), which slightly lower the α of trapped electrons. On the other hand, the $n < 1$ resonances cause decreasing of α, indicating that the trapped electrons move toward the loss cone.

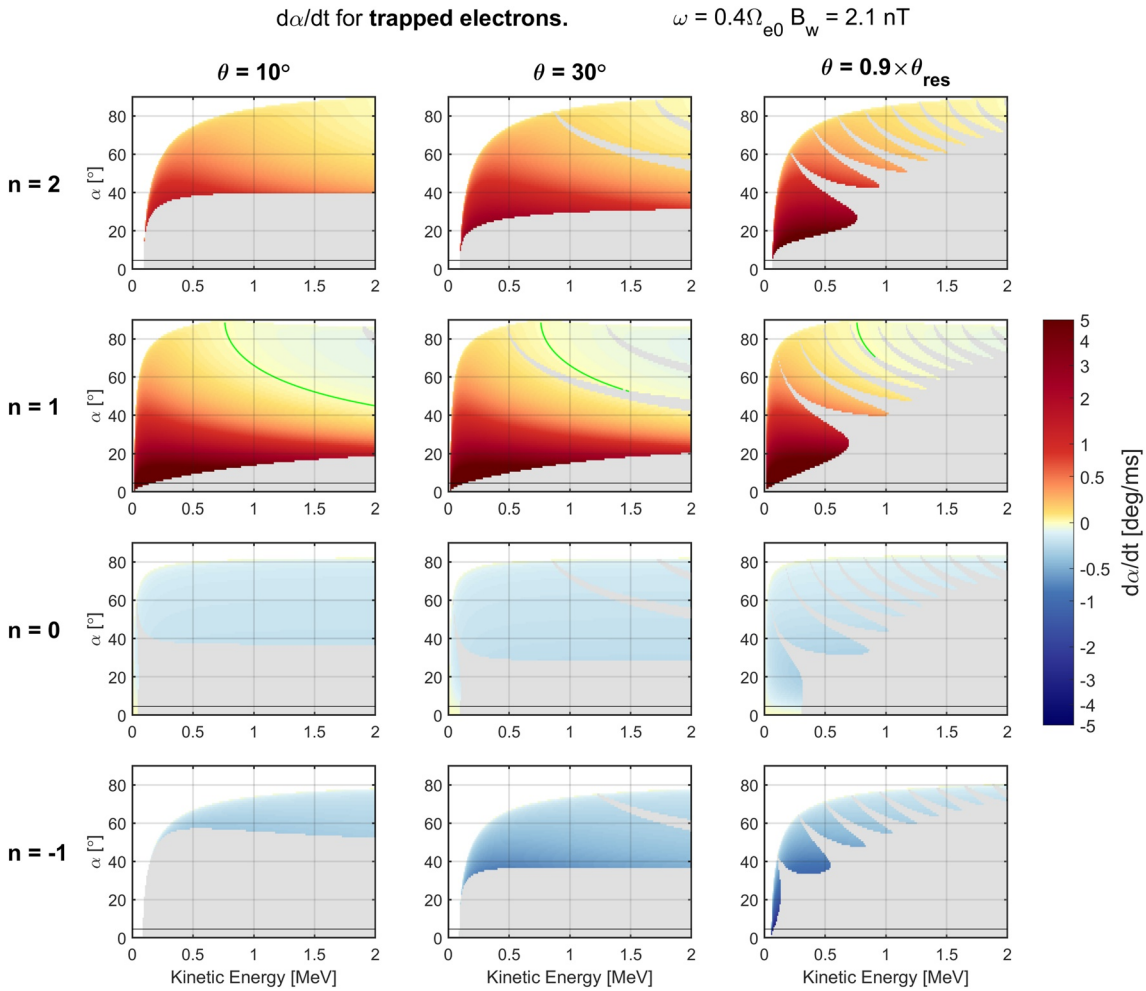

Figure 7. Equatorial pitch angle scattering rates of nonlinearly trapped electrons for a wave amplitude 2.1 nT and a wave frequency 0.4 Ω_{e0}. The figure configuration is the same as in Figure 6.

The most obvious parts in Figures 6 and 7 are the gray parts at low α in every sub-figure. For electrons with low α, $v_{\parallel} \simeq V_{Rn}$ usually occurs at high latitudes, where the $\partial\Omega/\partial h$ is too large to make $|S_n|$ less than unity. Low-energy (< tens of keV) electrons with the $n = 1$ cyclotron resonance and the $n = 0$ Landau resonance are exceptions. Precipitation implies that the equatorial pitch angle becomes smaller. For $\theta < 30°$ waves, precipitation is only caused by the $n = 0$ Landau resonance for electron <~50 keV, which is consistent with our previous study (Hsieh et al., 2022).

For the very oblique cases (the rightest column of Figures 6 and 7), electrons can be precipitated by the $n = 0$ Landau resonance at about 300 keV, which is higher than the other cases. Furthermore, the right-bottom plots of Figures 6 and 7 show that electrons have opportunities being pushed in to the loss cone by the $n = -1$ cyclotron resonance after interacting with a very oblique chorus wave. The $n = -1$ precipitation is much stronger than the $n = 0$ precipitation since the $d\alpha/dt$ of $n = -1$ resonance is much stronger than that of $n = 0$ resonance.

4.3. Untrapped Resonant Electrons

Figures 8 and 9 show $d\alpha/dt$ for nonlinearly scattered electrons with $\omega = 0.25\ \Omega_{e0}$ and $0.4\ \Omega_{e0}$, respectively. Untrapped electrons with different ζ_n have different $d\alpha/dt$. Here we plot the maximum $d\alpha/dt$ values. In the case with positive/negative S_n, we replace $\sin\zeta_n$ with $1/-1$, showing the different tendencies of equatorial pitch angle changes between nonlinearly scattered and nonlinearly trapped electrons.

Clearly, untrapped electrons via $n = 0$ and $n = -1$ resonances are not related to precipitation since the positive $d\alpha/dt$. The strong blue parts in the second row of Figures 8 and 9 indicate that the $n = 1$ cyclotron resonance causes electron precipitation in every case. However, we should notice that the interaction period is very short for

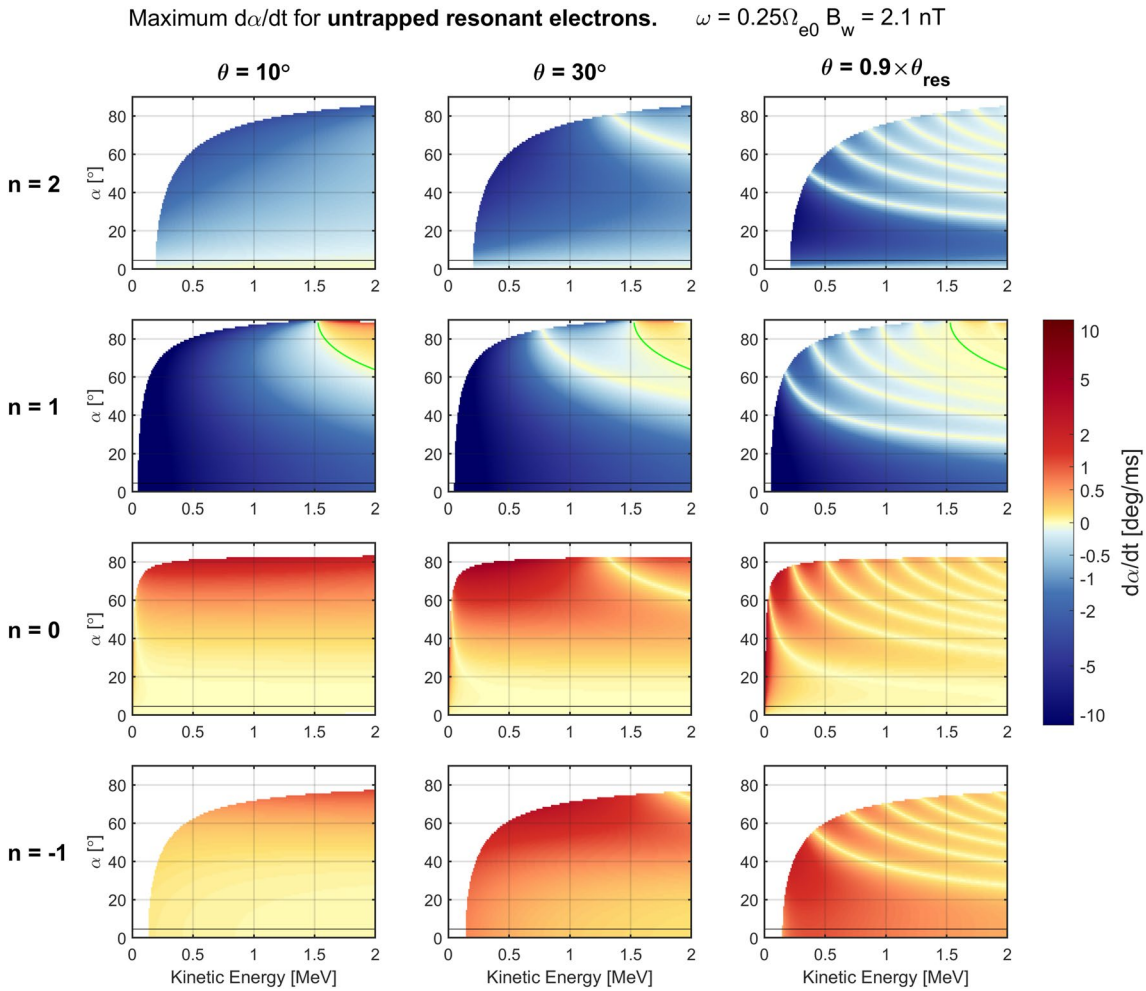

Figure 8. The maximum equatorial pitch angle scattering rates of untrapped electrons for a wave amplitude 2.1 nT and a wave frequency 0.25 Ω_{e0}. The figure configuration is the same as in Figure 6.

an untrapped electron, usually only a few ms. We can roughly calculate $\Delta\alpha$, which is $d\alpha/dt$ times the interaction period, for an untrapped electron to check if the wave and electron conditions can cause effective precipitation. If we calculate $\Delta\alpha$ from the values of $d\alpha/dt$ in Figures 8 and 9, we will find that the results do not consist with Figure 3. The calculated $\Delta\alpha$ should be too large. That is because the wave amplitudes in the simulation are not always the maximum values, and the $|\sin\zeta_n|$ of untrapped electrons should be less than 1. If we want to apply Equation 32 into other simulations or observations, we should be careful about the amplitude variations and the ζ_n. Nevertheless, the tendency $d\alpha/dt$ of $n = 1$ resonance is consistent with the HPA of Figure 3a (the parallel case), which shows that a higher $d\alpha/dt$ contribute to a higher HPA. Detailed comparisons between $d\alpha/dt$ and the simulated precipitation rates will be discussed later in Section 4.4.

4.4. Connections Between Simulated and Theoretical Electron Precipitation

In this section we compare the relation between simulation results shown in Section 3 and the $d\alpha/dt$. We only discuss the $B_{w,\max} = 2.1$ nT cases since they show strong nonlinear effects. Electron precipitation is directly connected to negative $d\alpha/dt$. Hence, we can say that the electron precipitation is caused by one or more of the following nonlinear processes:

1. Nonlinear scattering via $n = 1$ cyclotron resonance.
2. Nonlinear scattering via $n \geq 2$ resonance.
3. Nonlinear trapping via $n = 0$ Landau resonance.
4. Nonlinear trapping via $n = -1$ cyclotron resonance.

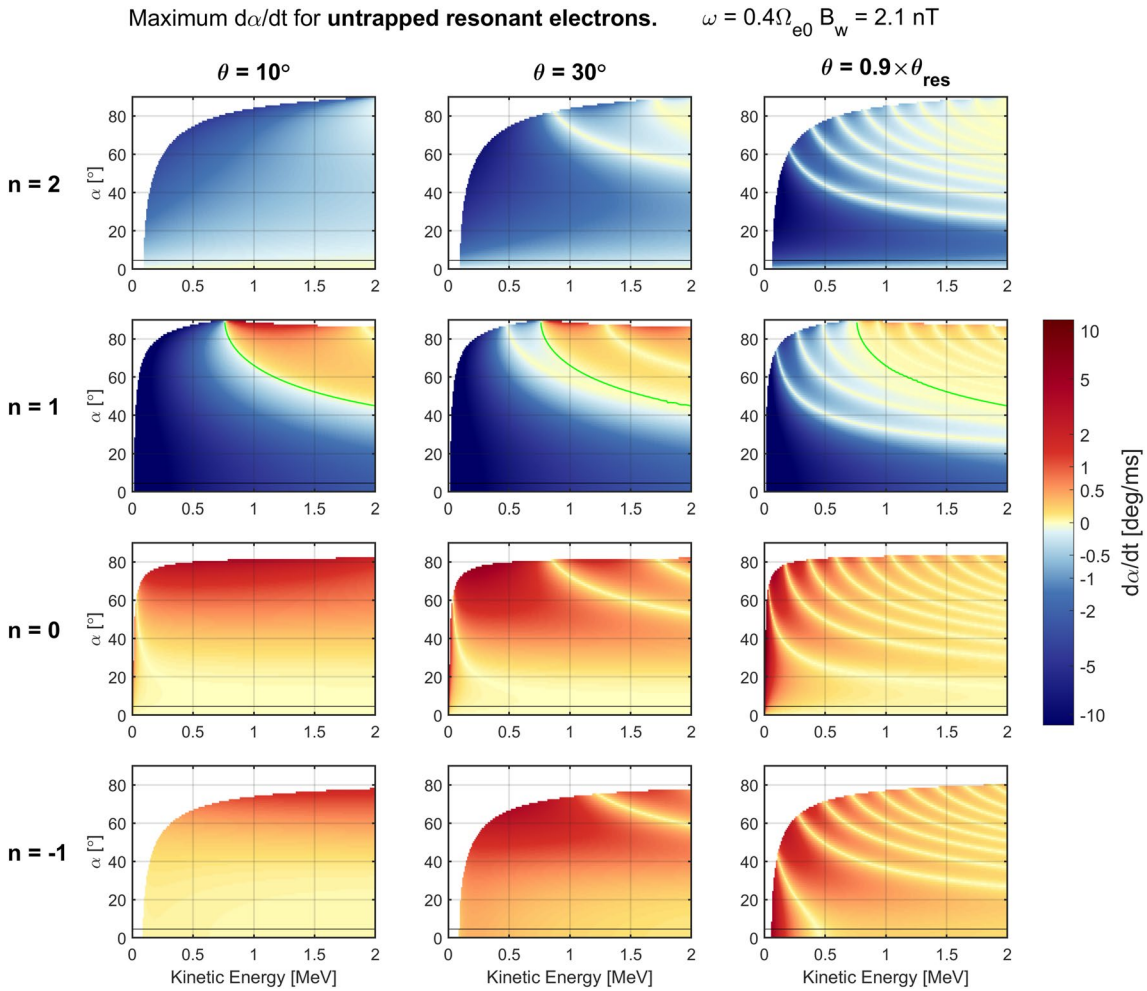

Figure 9. The maximum equatorial pitch angle scattering rates of untrapped electrons for a wave amplitude 2.1 nT and a wave frequency 0.25 Ω_{e0}. The figure configuration is the same as in Figure 6.

Note that the nonlinear trapping via $n = 1$ cyclotron resonance also results in negative $d\alpha/dt$ at high energies and high equatorial pitch angles (RTA and URA processes, usually occur around the equator), but the $d\alpha/dt$ is too small to let the electron drop into the loss cone from the high equatorial pitch angles. Therefore, precipitation done by the nonlinear trapping via $n = 1$ cyclotron resonance is impossible in a regular dipole magnetic field. Nonlinear trapping via $n < -1$ resonances is difficult to happen since the large $|S_n|$, so we do not discuss them in this study.

First, as mentioned in Section 4.3, the equatorial pitch angle scattering rates $d\alpha/dt$ of untrapped electrons agree with the majority of the precipitation rates in Figures 3a–3d (red parts). Figure 3e shows that the precipitation rates at energy $K < 30$ keV is lower than those at energy $K = 50$–100 keV. At these energy ranges, the nonlinear trapping effect, which scatters electrons to higher equatorial pitch angles, is also very strong (see the left-bottom part of the second row of Figures 6 and 7).

Second, about the bulges around $(K, \alpha) = (150$ keV, $20°)$ in Figures 3b and 3c and the extended cyan parts at $K > 300$ keV in Figures 3b–3d, they should be contributed by the $n = 2$ cyclotron resonance. The reasons are: (a) The $d\alpha/dt$ of the $n = 1$ resonance is almost the same in these 3 wave conditions, so there should be an additional process other than the $n = 1$ cyclotron resonance causing the bulges. (b) They are not caused by the nonlinear trapping via the $n = 0$ Landau resonance and the $n = -1$ cyclotron resonance because at these parts nonlinear trapping of $n < 1$ resonances can not occur (See Figures 6 and 7). (c) In Figures 8 and 9, the left boundaries of the $n = 2$ resonance parts agree with the energy of the precipitation bulges, supporting the conjecture that the $n = 2$ resonance contributes to the precipitation bulges (See the green dotted ovals in Figure 10).

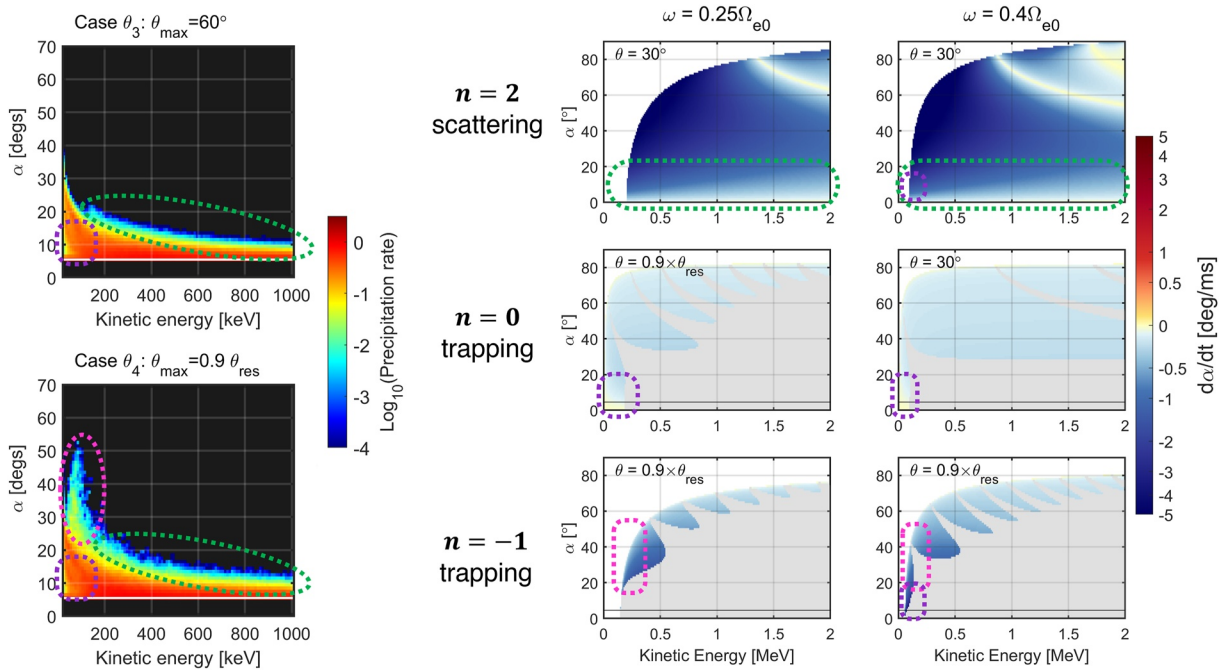

Figure 10. Connection of simulated precipitation rates (left panel) and theoretical dα/dt (right panel). The panels are from Figures 3 and 6–9.

Third, the nonlinear trapping of the $n = -1$ cyclotron resonance is the key process resulting in the distinct precipitation pattern around K = 30–150 keV and α = 30°–50° in Figure 3d (the very oblique case). Examining the dα/dt plots (Figures 6–9) we can find that the strong negative dα/dt at these K and α for trapped electrons undergoing the $n = -1$ cyclotron resonance only occurs with large wave amplitudes and very large WNAs. The precipitation can be the combined effect of multiple resonances, but without the $n = -1$ cyclotron resonance the electrons cannot precipitate from the equatorial pitch angles $\alpha > 40°$ (See the magenta dotted ovals in Figure 10).

Fourth, Figure 3e shows that the electron precipitation done by the oblique chorus emissions is higher than that done by the purely parallel chorus emissions at kinetic energies $K < 400$ keV. Three reasons contribute to this result: (a) The nonlinear trapping via the $n = 0$ Landau resonance slightly pushes low α electrons into the loss cone. (b) The nonlinear scattering via the $n = 2$ resonance also lower the equatorial pitch angles α of resonant electrons in this energy range. (c) The anomalous trapping of the $n = 1$ cyclotron resonance in the oblique WPI is weaker than that in the parallel WPI. The multiple resonances effect (including the $n = 0$ Landau resonance and the higher harmonic cyclotron resonances) reduces the number of low K and low α particles being transferred to high α. The above connections are shown as the purple dotted ovals in Figure 10. In addition, the precipitation rates of the very oblique chorus waves are higher than those of the parallel and the quasi-parallel chorus waves because of the strong $n = 0$ and $n = -1$ nonlinear trapping effects.

Consequently, we can say that electron precipitation induced by oblique chorus is more than that induced by parallel chorus if they have similar wave amplitudes and the amplitudes are large enough. Finding the threshold amplitude of effective precipitation by Landau resonance, and higher harmonic resonances remains as a future work.

4.5. Equatorial Pitch Angle Scattering Rates for B_w = 307 pT

We plot dα/dt for wave with B_w = 307 pT and ω = 0.4 Ω_{e0} in Figure 11 (trapped electrons) and Figure 12 (untrapped resonant electrons). Comparing Figure 7 with Figure 11, the gray areas are larger in the 307 pT cases than in the 2.1 nT cases, indicating that it is more difficult to have nonlinear trapping in the 307 pT cases. Values of dα/dt are much smaller in the 307 pT cases than in the 2.1 nT cases. Precipitation induced by the $n = -1$ cyclotron resonance is impossible, and that induced by the $n = 0$ Landau resonance is also very difficult. Also, values of dα/dt in Figure 12 are much smaller than in Figure 9. The maximum equatorial scattering rates of untrapped

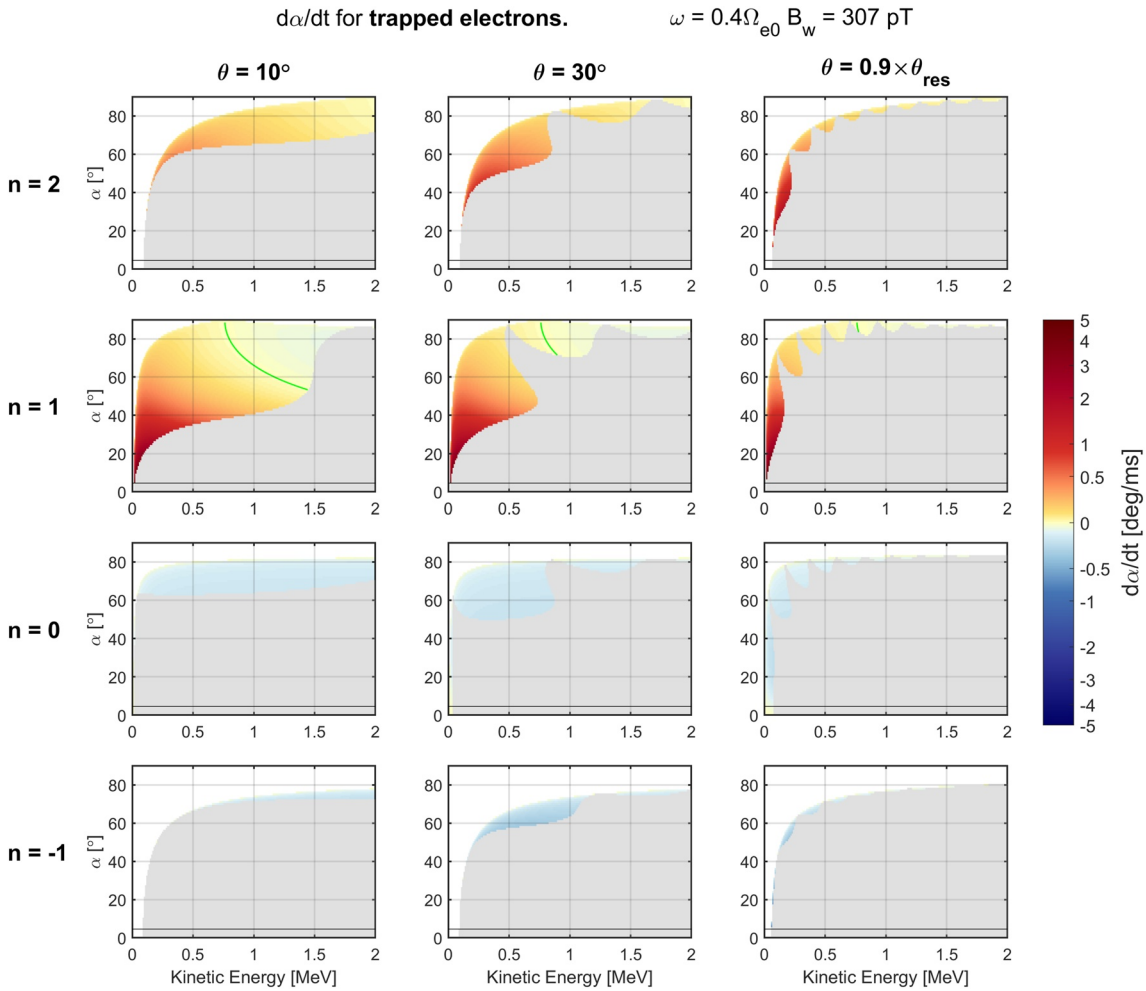

Figure 11. Equatorial pitch angle scattering rates of nonlinearly trapped electrons for a wave amplitude 300 pT and a wave frequency 0.4 Ω_{e0}. The figure configuration is the same as Figure 6.

resonant electrons are approximately proportional to the wave amplitudes. This comparison explains that the precipitation rates shown in Figure 5 have no apparent difference among different WNAs.

4.6. Efficiency of Electron Acceleration and Precipitation by Chorus Emissions

The precipitation rates among all pitch angles (Figure 3e) indicate that even if with large amplitudes, the largest precipitation rate is about 6%, which is much less than electrons trapped in the Earth's magnetic field. Hsieh et al. (2020, 2022) have demonstrated that oblique chorus emissions contribute to more accelerated electrons than precipitated electrons. Hence, we know that chorus emissions are not a good object to reduce the relativistic electrons in the radiation belts. EMIC waves, which does not cause electron energy changes during WPI, could work much effectively than chorus emissions in radiation belt electron losses (e.g., Kubota & Omura, 2017). Comparing the electron precipitation rates between chorus emissions and EMIC waves should worth checking as a future work.

5. Conclusions

In this study, we investigated the precipitation rates for electrons with energies 10–6,000 keV and equatorial pitch angles above the loss cone angles interacting with a pair of chorus emissions at an $L = 4.5$ field line. We applied 12 wave models with different wave amplitudes and WNAs. The electron precipitation rates are obtained from the Green's functions calculated by the test-particle simulations. We theoretically derived the equatorial pitch angle

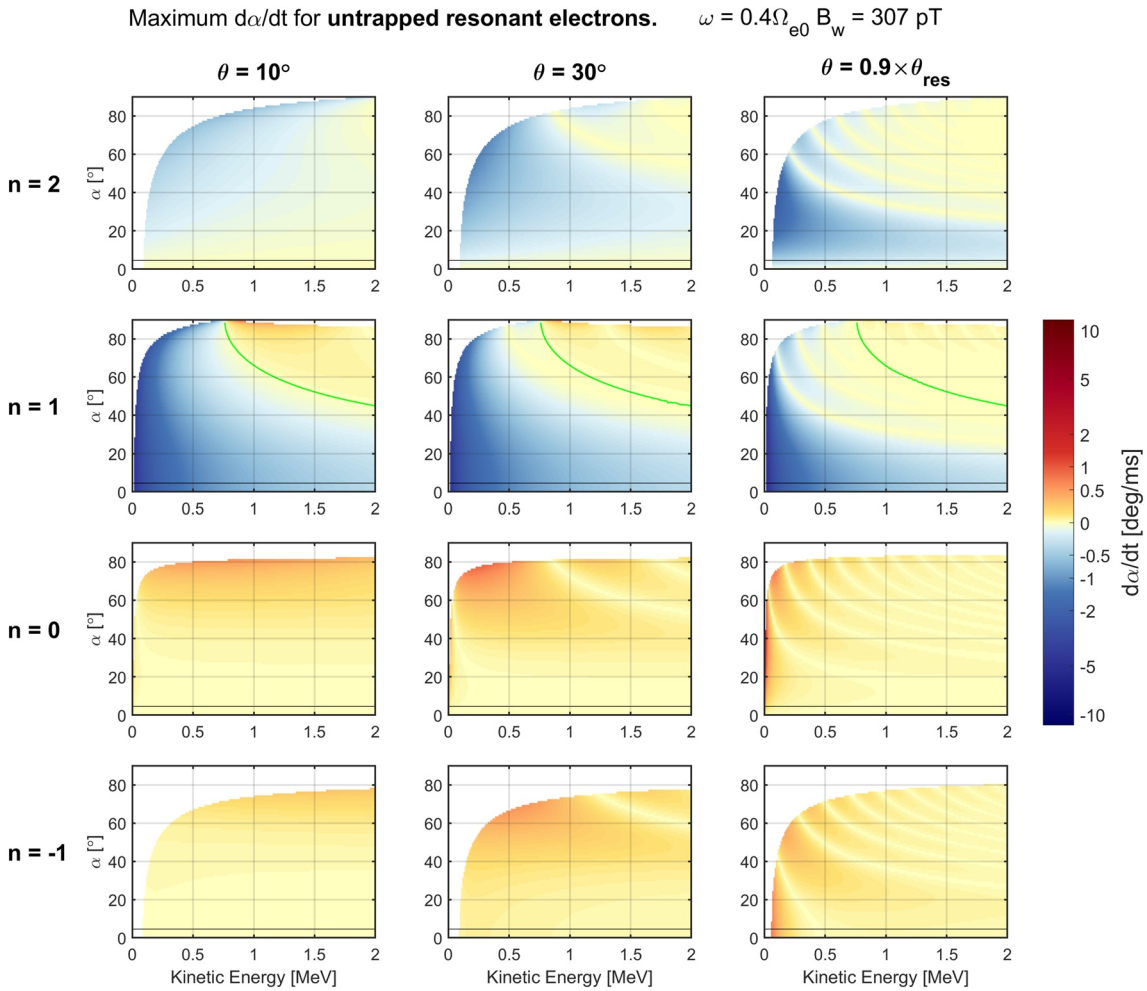

Figure 12. The maximum equatorial pitch angle scattering rates of untrapped electrons for a wave amplitude 307 pT and a wave frequency 0.4 Ω_{e0}. The figure configuration is the same as Figure 8.

scattering rates of resonant electrons and analyzed them in different wave amplitudes, wave frequencies, WNAs, and nth resonances. The physical findings are itemized as follows:

1. Wave amplitudes are the most important factor affecting energetic electron precipitation.
2. Under the same wave condition, in general, the precipitation rates of low-energy electrons are higher than those of high-energy electrons because the pitch angle scattering rates of the $n = 1$ cyclotron resonance is higher for low-energy electrons than for high-energy electrons.
3. For large amplitude waves, the precipitation rates of the very oblique chorus waves are about 1.5 times greater than those of the parallel waves and about 1.2 times greater than those of the slightly oblique waves. It is because of active nonlinear trapping ($n = 0$ and $n = -1$ resonances) and nonlinear scattering ($n = 2$ resonance).
4. In the large amplitude and very oblique case, electrons can precipitate from the initial equatorial pitch angles >40° around 100 keV because of the strong nonlinear trapping via the $n = -1$ cyclotron resonance.
5. The anomalous trapping effect is much weaker in the oblique cases than in the parallel cases.

When we observe a chorus event in the inner magnetosphere or in the outer radiation belt, we can obtain wave amplitudes, wave frequencies, WNAs, duration of wave subpackets, electron energies, electron pitch angles, the background magnetic field, and the equatorial background magnetic field. With these parameters, we can estimate the electron precipitation rates of the event by integrating Equation 32 over time. Then, the precipitation rates are helpful for determining whether the chorus event contributes to effective electron precipitation or not. This study only discussed the lower-band chorus emissions and did not take any upper-band chorus emissions

into account. Upper-band chorus emissions usually have larger WNAs and smaller wave amplitudes than lower-band chorus. We leave the upper-band chorus issue to future works.

Acronyms

WPI	Wave-particle interaction
WNA	Wave normal angle
HPA	Highest precipitation angles

Appendix A: Inhomogeneity Factor for Oblique Whistler Mode Wave-Particle Interactions

Omura et al. (2019) has already provided the equation inhomogeneity factor S_n for different nth resonances, but it assumed a small WNA and applied parallel dispersion relation in the derivation. Therefore, it is not available for all oblique chorus emissions. Here we directly use the dispersion relation of oblique whistler mode waves to derive the inhomogeneity factor.

Derivation of the inhomogeneity factor starts from equations of motion (Equations 5–7). With the Bessel function expansions, the equations of motion can be written as

$$\frac{dv_\parallel}{dt} = \frac{1}{\gamma k_\parallel}\sum_{n=-\infty}^{\infty}\left(\omega_{t,n}^2 - \frac{v_\parallel k_\parallel W_n}{c^2}\right)\sin\zeta_n - \frac{\gamma v_\perp^2}{2\Omega_e}\frac{d\Omega_e}{dh}, \tag{A1}$$

$$\frac{dv_\perp}{dt} = \frac{1}{\gamma k_\parallel}\sum_{n=-\infty}^{\infty}\left(\omega_{s,n}^2 - \frac{v_\perp k_\parallel W_n}{c^2}\right)\sin\zeta_n + \frac{\gamma v_\perp v_\parallel}{2\Omega_e}\frac{d\Omega_e}{dh}, \tag{A2}$$

and

$$\frac{d\phi}{dt} = \frac{\Omega_e}{\gamma} + \frac{1}{\gamma}\sum_{n=-\infty}^{\infty}\omega_{f,n}\cos\zeta_n, \tag{A3}$$

where

$$\omega_{f,n} = \frac{\Omega_R}{v_\perp}(U_R - v_\parallel)J_{n-1}(\beta) + \frac{\Omega_L}{v_\perp}(U_L - v_\parallel)J_{n+1}(\beta) - \Omega_\parallel J_n(\beta). \tag{A4}$$

Time derivative of the wave phase at guiding center is

$$\frac{d\phi_B}{dt} = \omega - k_\parallel v_\parallel. \tag{A5}$$

Then, time derivative of ζ_n is written as

$$\begin{aligned}\frac{d\zeta_n}{dt} &= n\frac{d\phi}{dt} - \frac{d\phi_B}{dt}\\ &= k_\parallel(v_\parallel - V_{R,n}) + \frac{n}{\gamma}\sum_{n=-\infty}^{\infty}\omega_{f,n}\cos\zeta_n.\end{aligned} \tag{A6}$$

The first term of Equation A6 is the nth resonance term and the second term is anomalous trapping term, which is important when the local equatorial pitch angle is very small or the wave amplitude is large. Ignoring the anomalous trapping term, the time derivative of Equation A6 is

$$\begin{aligned}\frac{d^2\zeta_n}{dt^2} &= \frac{d}{dt}\left(k_\parallel v_\parallel - \omega + \frac{n\Omega_e}{\gamma}\right)\\ &= k_\parallel\frac{dv_\parallel}{dt} + v_\parallel\frac{k_\parallel}{dt} - \frac{d\omega}{dt} + \frac{n}{\gamma}\frac{d\Omega_e}{dt} - \frac{n\Omega_e}{\gamma^2}\frac{d\gamma}{dt}.\end{aligned} \tag{A7}$$

Time derivatives of ω, $k_\parallel$, and Ω_e are given by

$$\frac{d\omega}{dt} \simeq \frac{\partial\omega}{\partial t} + v_\parallel\frac{\partial\omega}{\partial h} = \left(1 - \frac{v_\parallel}{V_{g\parallel}}\right)\frac{\partial\omega}{\partial t}, \tag{A8}$$

$$\frac{\mathrm{d}k_{\parallel}}{\mathrm{d}t} \simeq \frac{\partial k_{\parallel}}{\partial t} + v_{\parallel}\frac{\partial k_{\parallel}}{\partial h} = \frac{1}{V_{g\parallel}}\frac{\partial \omega}{\partial t} + v_{\parallel}\frac{\partial k_{\parallel}}{\partial h}, \tag{A9}$$

$$\frac{\mathrm{d}\Omega_e}{\mathrm{d}t} = v_{\parallel}\frac{\partial \Omega_e}{\partial h}. \tag{A10}$$

Substituting Equations 21–24 and A8–A10 into Equation A7, and only consider the nth resonance, we obtain

$$\begin{aligned}\frac{\mathrm{d}^2\zeta_n}{\mathrm{d}t^2} &= \frac{1}{\gamma}\left[\omega_{t,n}^2 - \left(k_{\parallel}v_{\parallel} - \frac{n\Omega_e}{\gamma}\right)\Omega_{d,n}\right]\sin\zeta_n + \left(\frac{2v_{\parallel}}{V_{g\parallel}} - 1\right)\frac{\partial \omega}{\partial t} + v_{\parallel}^2\frac{\partial k_{\parallel}}{\partial h} + \left(\frac{n}{\gamma}v_{\parallel} - \frac{k_{\parallel}v_{\perp}^2}{2\Omega_e}\right)\frac{\partial \Omega_e}{\partial h} \\ &= \Omega_{t,n}^2(\sin\zeta_n + S_n).\end{aligned} \tag{A11}$$

According to Equation A11, we know that

$$\Omega_{t,n}^2 = \frac{1}{\gamma}\left[\omega_{t,n}^2 - \left(k_{\parallel}v_{\parallel} - \frac{n\Omega_e}{\gamma}\right)\Omega_{d,n}\right], \tag{A12}$$

$$S_n = \frac{1}{\Omega_{t,n}^2}\left[\left(\frac{2v_{\parallel}}{V_{g\parallel}} - 1\right)\frac{\partial \omega}{\partial t} + v_{\parallel}^2\frac{\partial k_{\parallel}}{\partial h} + \left(\frac{n}{\gamma}v_{\parallel} - \frac{k_{\parallel}v_{\perp}^2}{2\Omega_e}\right)\frac{\partial \Omega_e}{\partial h}\right], \tag{A13}$$

which is the nth inhomogeneity factor for any electrons. The frequency sweep rate affects the first and second terms in the square brackets, and the gradient of the background contributes to the second and third terms. The second term is also affected by spatial distribution of plasma frequency and WNA.

If $v_{\parallel} \simeq V_{R,n}$, we have the values for resonant electrons as

$$\Omega_{t,n}^2 = \frac{1}{\gamma}\left(\omega_{t,n}^2 - \omega\Omega_{d,n}\right), \tag{A14}$$

$$S_n = \frac{1}{\Omega_{t,n}^2}\left[\left(\frac{2V_{R,n}}{V_{g\parallel}} - 1\right)\frac{\partial \omega}{\partial t} + V_{R,n}^2\frac{\partial k_{\parallel}}{\partial h} + \left(\frac{n}{\gamma}V_{R,n} - \frac{k_{\parallel}v_{\perp}^2}{2\Omega_e}\right)\frac{\partial \Omega_e}{\partial h}\right]. \tag{A15}$$

For observations, it is difficult to obtain $\partial k_{\parallel}/\partial h$ for a rising tone or falling tone chorus emission, but we can obtain $\partial\Omega_e/\partial h$ and $\partial\omega_{pe}/\partial h$ from models of the background magnetic and plasma density. Therefore, assuming WNA θ, electron plasma frequency ω_{pe}, and the background magnetic field are only functions of position h, we have

$$\frac{\partial k_{\parallel}}{\partial h} = \frac{\partial k_{\parallel}}{\partial \omega}\frac{\partial \omega}{\partial h} + \frac{\partial k_{\parallel}}{\partial \theta}\frac{\partial \theta}{\partial h} + \frac{\partial k_{\parallel}}{\partial \omega_{pe}}\frac{\partial \omega_{pe}}{\partial h} + \frac{\partial k_{\parallel}}{\partial \Omega_e}\frac{\partial \Omega_e}{\partial h} \tag{A16}$$

$$= \frac{1}{V_{g\parallel}^2}\left(-\frac{\partial \omega}{\partial t}\right) + \frac{\partial k_{\parallel,c}}{\partial h}, \tag{A17}$$

where $\partial k_{\parallel,c}/\partial h = \frac{\partial k_{\parallel}}{\partial \theta}\frac{\partial \theta}{\partial h} + \frac{\partial k_{\parallel}}{\partial \omega_{pe}}\frac{\partial \omega_{pe}}{\partial h} + \frac{\partial k_{\parallel}}{\partial \Omega_e}\frac{\partial \Omega_e}{\partial h}$ is derived from the background models with the oblique whistler mode dispersion relation (Hsieh & Omura, 2017) and a constant wave frequency ω. Then, Equation A15 is rewritten as

$$S_n = \frac{1}{\Omega_{t,n}^2}\left[-\left(\frac{V_{R,n}}{V_{g\parallel}} - 1\right)^2\frac{\partial \omega}{\partial t} + V_{R,n}^2\frac{\partial k_{\parallel,c}}{\partial h} + \left(\frac{n}{\gamma}V_{R,n} - \frac{k_{\parallel}v_{\perp}^2}{2\Omega_e}\right)\frac{\partial \Omega_e}{\partial h}\right]. \tag{A18}$$

If we ignore the gradient of WNAs and the gradient of plasma frequencies and apply the quasi-longitudinal approximation

$$\frac{c^2k^2}{\omega^2} = \frac{(\omega_{pe}/\omega)^2}{\frac{\Omega_e}{\omega}\cos\theta - 1} \tag{A19}$$

into the dispersion relation, S_n can be simply written as a function of the frequency sweep rate and the background magnetic field gradient as

$$S_n = \frac{1}{\Omega_{t,n}^2}\left\{-\left(\frac{V_{R,n}}{V_{g\parallel}}-1\right)^2\frac{\partial\omega}{\partial t}+\left[\frac{n}{\gamma}V_{R,n}-\frac{k_\parallel v_\perp^2}{2\Omega_e}-\frac{V_{R,n}^2}{2}\left(\frac{\omega_{pe}}{c}\right)^3\left(\frac{\Omega_e}{\omega}\cos\theta-1\right)^{-\frac{3}{2}}\frac{\cos^2\theta}{\omega}\right]\frac{\partial\Omega_e}{\partial h}\right\}, \quad \text{(A20)}$$

which is useful for roughly estimating S_n in observations.

Data Availability Statement

The simulation data used in this paper are obtained from numerical integration of Equation 4 by the Buneman-Boris method. Simulation data (Hsieh, 2022) is accessible at repository https://doi.org/10.5281/zenodo.7475801.

Acknowledgments
The computer simulation was performed on the A-KDK computer system at Research Institute for Sustainable Humanosphere, Kyoto University. This work was supported by JSPS KAKENHI Grants JP17H06140, JP20H01960, and JP22K21345.

References

Agapitov, O., Mourenas, D., Artemyev, A., Mozer, F., Bonnell, J., Angelopoulos, V., et al. (2018). Spatial extent and temporal correlation of chorus and hiss: Statistical results from multipoint themis observations. *Journal of Geophysical Research: Space Physics*, *123*(10), 8317–8330. https://doi.org/10.1029/2018JA025725

Artemyev, A., Zhang, X.-J., Zou, Y., Mourenas, D., Angelopoulos, V., Vainchtein, D., et al. (2022). On the nature of intense sub-relativistic electron precipitation. *Journal of Geophysical Research: Space Physics*, *127*(6), e2022JA030571. https://doi.org/10.1029/2022JA030571

Bashir, M. F., Artemyev, A., Zhang, X.-J., & Angelopoulos, V. (2022). Energetic electron precipitation driven by the combined effect of ULF, EMIC, and whistler waves. *Journal of Geophysical Research: Space Physics*, *127*(1), e2021JA029871. https://doi.org/10.1029/2021JA029871

Bortnik, J., Thorne, R., & Inan, U. S. (2008). Nonlinear interaction of energetic electrons with large amplitude chorus. *Geophysical Research Letters*, *35*(21), L21102. https://doi.org/10.1029/2008GL035500

Breneman, A., Crew, A., Sample, J., Klumpar, D., Johnson, A., Agapitov, O., et al. (2017). Observations directly linking relativistic electron microbursts to whistler mode chorus: Van Allen Probes and FIREBIRD II. *Geophysical Research Letters*, *44*(22), 11–265. https://doi.org/10.1002/2017GL075001

Breneman, A. W., Kletzing, C. A., Pickett, J., Chum, J., & Santolik, O. (2009). Statistics of multispacecraft observations of chorus dispersion and source location. *Journal of Geophysical Research*, *114*(A6), A05215. https://doi.org/10.1029/2008JA013549

Chen, L., Zhang, X.-J., Artemyev, A., Zheng, L., Xia, Z., Breneman, A. W., & Horne, R. B. (2021). Electron microbursts induced by nonducted chorus waves. *Frontiers in Astronomy and Space Sciences*, *8*, 745927. https://doi.org/10.3389/fspas.2021.745927

Foster, J., Erickson, P., Omura, Y., Baker, D., Kletzing, C., & Claudepierre, S. (2017). Van Allen Probes observations of prompt MeV radiation belt electron acceleration in nonlinear interactions with VLF chorus. *Journal of Geophysical Research: Space Physics*, *122*(1), 324–339. https://doi.org/10.1002/2016JA023429

Grach, S. V., & Demekhov, A. G. (2020). Precipitation of relativistic electrons under resonant interaction with electromagnetic ion cyclotron wave packets. *Journal of Geophysical Research: Space Physics*, *125*(2), e2019JA027358. https://doi.org/10.1029/2019JA027358

Hikishima, M., Omura, Y., & Summers, D. (2010). Microburst precipitation of energetic electrons associated with chorus wave generation. *Geophysical Research Letters*, *37*(7), L07103. https://doi.org/10.1029/2010GL042678

Hsieh, Y.-K. (2022). Data set of precipitation rates of electrons interacting with lower-band chorus emissions in the inner magnetosphere [dataset]. Zenodo. https://doi.org/10.5281/zenodo.7475801

Hsieh, Y.-K., Kubota, Y., & Omura, Y. (2020). Nonlinear evolution of radiation belt electron fluxes interacting with oblique whistler mode chorus emissions. *Journal of Geophysical Research: Space Physics*, *125*(2), e2019JA027465. https://doi.org/10.1029/2019JA027465

Hsieh, Y.-K., & Omura, Y. (2017). Nonlinear dynamics of electrons interacting with oblique whistler mode chorus in the magnetosphere. *Journal of Geophysical Research: Space Physics*, *122*(1), 675–694. https://doi.org/10.1002/2016JA023255

Hsieh, Y.-K., Omura, Y., & Kubota, Y. (2022). Energetic electron precipitation induced by oblique whistler mode chorus emissions. *Journal of Geophysical Research: Space Physics*, *127*(1), e2021JA029583. https://doi.org/10.1029/2021JA029583

Kasahara, S., Miyoshi, Y., Yokota, S., Mitani, T., Kasahara, Y., Matsuda, S., et al. (2018). Pulsating aurora from electron scattering by chorus waves. *Nature*, *554*(7692), 337–340. https://doi.org/10.1038/nature25505

Kitahara, M., & Katoh, Y. (2019). Anomalous trapping of low pitch angle electrons by coherent whistler mode waves. *Journal of Geophysical Research: Space Physics*, *124*(7), 5568–5583. https://doi.org/10.1029/2019JA026493

Kubota, Y., & Omura, Y. (2017). Rapid precipitation of radiation belt electrons induced by emic rising tone emissions localized in longitude inside and outside the plasmapause. *Journal of Geophysical Research: Space Physics*, *122*(1), 293–309. https://doi.org/10.1002/2016JA023267

Kubota, Y., & Omura, Y. (2018). Nonlinear dynamics of radiation belt electrons interacting with chorus emissions localized in longitude. *Journal of Geophysical Research: Space Physics*, *123*(6), 4835–4857. https://doi.org/10.1029/2017JA025050

Kurita, S., Miyoshi, Y., Blake, J. B., Reeves, G. D., & Kletzing, C. A. (2016). Relativistic electron microbursts and variations in trapped mev electron fluxes during the 8–9 October 2012 storm: SAMPEX and Van Allen Probes observations. *Geophysical Research Letters*, *43*(7), 3017–3025. https://doi.org/10.1002/2016GL068260

Li, W., Bortnik, J., Thorne, R., & Angelopoulos, V. (2011). Global distribution of wave amplitudes and wave normal angles of chorus waves using THEMIS wave observations. *Journal of Geophysical Research*, *116*(A12), A12205. https://doi.org/10.1029/2011JA017035

Lorentzen, K., Blake, J., Inan, U., & Bortnik, J. (2001). Observations of relativistic electron microbursts in association with VLF chorus. *Journal of Geophysical Research*, *106*(A4), 6017–6027. https://doi.org/10.1029/2000JA003018

Lyons, L. R., Thorne, R. M., & Kennel, C. F. (1972). Pitch-angle diffusion of radiation belt electrons within the plasmasphere. *Journal of Geophysical Research*, *77*(19), 3455–3474. https://doi.org/10.1029/JA077i019p03455

Ma, Q., Artemyev, A., Mourenas, D., Li, W., Thorne, R., Kletzing, C., et al. (2017). Very oblique whistler mode propagation in the radiation belts: Effects of hot plasma and landau damping. *Geophysical Research Letters*, *44*(24), 12–057. https://doi.org/10.1002/2017GL075892

Miyoshi, Y., Hosokawa, K., Kurita, S., Oyama, S.-I., Ogawa, Y., Saito, S., et al. (2021). Penetration of MeV electrons into the mesosphere accompanying pulsating aurorae. *Scientific Reports*, *11*(1), 1–9. https://doi.org/10.1038/s41598-021-92611-3

Mourenas, D., Artemyev, A., Agapitov, O., Krasnoselskikh, V., & Li, W. (2014). Approximate analytical solutions for the trapped electron distribution due to quasi-linear diffusion by whistler mode waves. *Journal of Geophysical Research: Space Physics*, *119*(12), 9962–9977. https://doi.org/10.1002/2014JA020443

Mourenas, D., Artemyev, A., Agapitov, O., Krasnoselskikh, V., & Mozer, F. (2015). Very oblique whistler generation by low-energy electron streams. *Journal of Geophysical Research: Space Physics*, *120*(5), 3665–3683. https://doi.org/10.1002/2015JA021135

Nishimura, Y., Bortnik, J., Li, W., Thorne, R. M., Lyons, L. R., Angelopoulos, V., et al. (2010). Identifying the driver of pulsating aurora. *Science*, *330*(6000), 81–84. https://doi.org/10.1126/science.1193186

Nunn, D. (1974). A self-consistent theory of triggered VLF emissions. *Planetary and Space Science*, *22*(3), 349–378. https://doi.org/10.1016/0032-0633(74)90070-1

Nunn, D., & Omura, Y. (2015). A computational and theoretical investigation of nonlinear wave-particle interactions in oblique whistlers. *Journal of Geophysical Research: Space Physics*, *120*(4), 2890–2911. https://doi.org/10.1002/2014JA020898

Omura, Y. (2021). Nonlinear wave growth theory of whistler-mode chorus and hiss emissions in the magnetosphere. *Earth Planets and Space*, *73*(1), 1–28. https://doi.org/10.1186/s40623-021-01380-w

Omura, Y., Furuya, N., & Summers, D. (2007). Relativistic turning acceleration of resonant electrons by coherent whistler mode waves in a dipole magnetic field. *Journal of Geophysical Research*, *112*(A6), 12. https://doi.org/10.1029/2006JA012243

Omura, Y., Hikishima, M., Katoh, Y., Summers, D., & Yagitani, S. (2009). Nonlinear mechanisms of lower-band and upper-band VLF chorus emissions in the magnetosphere. *Journal of Geophysical Research*, *114*(A7), A07217. https://doi.org/10.1029/2009JA014206

Omura, Y., Hsieh, Y.-K., Foster, J. C., Erickson, P. J., Kletzing, C. A., & Baker, D. N. (2019). Cyclotron acceleration of relativistic electrons through landau resonance with obliquely propagating whistler-mode chorus emissions. *Journal of Geophysical Research: Space Physics*, *124*(4), 2795–2810. https://doi.org/10.1029/2018JA026374

Omura, Y., Miyashita, Y., Yoshikawa, M., Summers, D., Hikishima, M., Ebihara, Y., & Kubota, Y. (2015). Formation process of relativistic electron flux through interaction with chorus emissions in the Earth's inner magnetosphere. *Journal of Geophysical Research: Space Physics*, *120*(11), 9545–9562. https://doi.org/10.1002/2015JA021563

Ozaki, M., Miyoshi, Y., Shiokawa, K., Hosokawa, K., Oyama, S.-I., Kataoka, R., et al. (2019). Visualization of rapid electron precipitation via chorus element wave–particle interactions. *Nature Communications*, *10*(1), 1–9. https://doi.org/10.1038/s41467-018-07996-z

Rae, I. J., Murphy, K. R., Watt, C. E., Halford, A. J., Mann, I. R., Ozeke, L. G., et al. (2018). The role of localized compressional ultra-low frequency waves in energetic electron precipitation. *Journal of Geophysical Research: Space Physics*, *123*(3), 1900–1914. https://doi.org/10.1002/2017JA024674

Saito, S., Miyoshi, Y., & Seki, K. (2012). Relativistic electron microbursts associated with whistler chorus rising tone elements: GEMSIS-RBW simulations. *Journal of Geophysical Research*, *117*(A10), 10206. https://doi.org/10.1029/2012JA018020

Santolík, O., Kletzing, C., Kurth, W., Hospodarsky, G., & Bounds, S. (2014). Fine structure of large-amplitude chorus wave packets. *Geophysical Research Letters*, *41*(2), 293–299. https://doi.org/10.1002/2013GL058889

Sazhin, S., & Hayakawa, M. (1992). Magnetospheric chorus emissions: A review. *Planetary and Space Science*, *40*(5), 681–697. https://doi.org/10.1016/0032-0633(92)90009-D

Shprits, Y. Y., Subbotin, D. A., Meredith, N. P., & Elkington, S. R. (2008). Review of modeling of losses and sources of relativistic electrons in the outer radiation belt II: Local acceleration and loss. *Journal of Atmospheric and Solar-Terrestrial Physics*, *70*(14), 1694–1713. https://doi.org/10.1016/j.jastp.2008.06.014

Shue, J.-H., Nariyuki, Y., Katoh, Y., Saito, S., Kasahara, Y., Hsieh, Y.-K., et al. (2019). A systematic study in characteristics of lower band rising-tone chorus elements. *Journal of Geophysical Research: Space Physics*, *124*(11), 9003–9016. https://doi.org/10.1029/2019JA027368

Summers, D., & Omura, Y. (2007). Ultra-relativistic acceleration of electrons in planetary magnetospheres. *Geophysical Research Letters*, *34*(24), L24205. https://doi.org/10.1029/2007GL032226

Thorne, R. M., O'Brien, T., Shprits, Y., Summers, D., & Horne, R. B. (2005). Timescale for MeV electron microburst loss during geomagnetic storms. *Journal of Geophysical Research*, *110*(A9), 9202. https://doi.org/10.1029/2004JA010882

Tsai, E., Artemyev, A., Zhang, X.-J., & Angelopoulos, V. (2022). Relativistic electron precipitation driven by nonlinear resonance with whistler-mode waves. *Journal of Geophysical Research: Space Physics*, *127*(5), e2022JA030338. https://doi.org/10.1029/2022JA030338

Zhang, X.-J., Artemyev, A., Angelopoulos, V., Tsai, E., Wilkins, C., Kasahara, S., et al. (2022). Superfast precipitation of energetic electrons in the radiation belts of the Earth. *Nature Communications*, *13*(1), 1–8. https://doi.org/10.1038/s41467-022-29291-8

Zhang, X.-J., Mourenas, D., Artemyev, A., Angelopoulos, V., & Sauvaud, J.-A. (2019). Precipitation of MeV and sub-MeV electrons due to combined effects of EMIC and ULF waves. *Journal of Geophysical Research: Space Physics*, *124*(10), 7923–7935. https://doi.org/10.1029/2019JA026566